# Energy radiation from intermediate to large magnitude earthquakes: implications for dynamic fault weakening

by Luca Malagnini[1*], Stefan Nielsen[1], Kevin Mayeda[2], and Enzo Boschi[1]

[1] *Istituto Nazionale di Geofisica e Vulcanologia, Rome, Italy*

[2] *Weston Geophysical Corporation, Lexington, MA, and University of California, Berkeley, CA*

[*] To whom correspondence should be addressed; e-mail: luca.malagnini@ingv.it

## Abstract

The amount of energy radiated from an earthquake can be measured using recent methods based on earthquake coda signals and spectral ratios. Such methods are not altered by either site or directivity effects, with the advantage of a greatly improved accuracy. Several studies of earthquake sequences based on the above measurements showed evidence of a breakdown in self-similarity in the moment to energy relation. Radiated energy can be also used as a gauge to estimate the average dynamic stress drop on the fault. Here we compute the dynamic stress drop, infer the co-seismic friction and estimate the co-seismic heating resulting from the frictional work during events from different main shock-aftershock earthquake sequences. We relate the dynamic friction to the maximum temperature rise estimated on the faults for each earthquake. Our results are strongly indicative that a thermally triggered dynamic frictional weakening is present, responsible for the breakdown in self-similarity. These observations from seismic data are compatible with recent laboratory evidence of thermal weakening in rock friction under seismic slip-rates, associated to various physical processes such as melting, decarbonation or dehydration.

## Introduction

Whether earthquakes show a strict self-similar scaling (Ide and Beroza, 2001), or whether they obey a more complex scaling law (Izutani, 2005) is still an open debate in the seismological community (poll results of the 2005 Chapman Conference on Radiated Energy and the Physics of Earthquake Faulting: https://eed.llnl.gov/scaling-workshop/pdf/BWalter_Intro.pdf).

Both models may actually apply, with departures from self-similarity in some mainshock/aftershocks sequences but not in others (Mayeda and Malagnini, 2009). The difficulty in discriminating between the two models is in great part due to the lack of precision of the classic tools that may be used for determining earthquake energies and sizes (Mayeda et al., 2007). In addition, trivial variations in fault behavior due to changes in lithology or faulting type may be rather large and hinder unusual variations in the scaling. This last point may be improved by comparing only earthquakes generated within the same fault region or fault zone, with the disadvantage of reducing the available catalog and of working on a much smaller group of earthquakes at a time.

Very small earthquakes (Mw< 2) may be characterized by extreme static stress drops: 200 MPa or more have been estimated from repeating earthquakes by Nadeau and Johnson (1998), whereas Griffith et al. (2009), showing evidence of fossil seismicity, inferred large static stress drops for small faults affecting mostly fresh rocks. However, we do not consider those end members here, but rather earthquake sequences with magnitudes in the range ($3.8<M_w<7.6$). Among these, in the cases where self-similarity does not hold, larger events generally appear to have a relatively larger radiated energy (normalized to moment); simple scaling laws are not strictly obeyed, indicating that either the static or the dynamic properties of the fault somehow depend on the earthquake's magnitude. Among others, we may conjecture the occurrence of a systematic variation with magnitude either of rupture velocity, or of high frequency radiation due to fault complexity, or of initial stress on the fault. Any of the above properties, indeed, affects the relative amount of radiated energy. However, a systematic variation in either rupture velocity or fault complexity is difficult to justify, while a variation in the initial stress seems more reasonable. For example, smaller events may belong to aftershocks triggered on weaker neighboring faults, after the principal stress direction became more favorably oriented, or after the pore pressure increased in the vicinity of the fault, as a consequence of the main shock. In addition, one may argue that the apparent energy increase with magnitude is an artifact due to bandwidth limitations (smaller events may have part of the higher frequency attenuated or poorly sampled) and great care should be taken in verifying this issue.

Finally, one straightforward interpretation of the fact that larger earthquakes appear to radiate more energy (per unit fault area, per unit slip) is that larger earthquakes are characterized by a lower residual friction, because faults are progressively weakening under dynamic slip, resulting in an increased dynamic stress drop for events with a larger slip. Here, we explore the consequences of the latter interpretation in terms of the friction dynamics of faults and leave aside other possible interpretations for future studies.

Numerous mechanisms have been invoked to quantitatively describe the dynamic weakening of faults: acoustic fluidization (Melosh, 1996), elastohydrodynamic lubrication (Brodsky and Kanamori, 2001), pore fluid thermal pressurization (Rempel and Rice, 2006), flash heating (Rice, 2006), decarbonation with formation of nanopowders (Han et al, 2007), dehydration (Hirose and Bystricky, 2007), formation of gel (Di Toro et al., 2004), frictional melt (Nielsen et al., 2008), and coseismic fluid pressurization due to frictional $CO_2$ exsolution (Famin et al., 2008); a number of them were reproduced in laboratory experiments (Han et al., 2007; Hirose and Bystricky, 2007; Di Toro et al., 2004; Nielsen et al., 2008; Famin et al., 2008). Most of these mechanisms are triggered by frictional heating and, thus, enhanced weakening should prevail whenever a large slip occurs in a short time (Rice, 2006; Nielsen et al., 2008, Famin et al., 2008). Seismic events that release more heat are those where a larger stress drop is expected (Madariaga, 2007), so that the breakdown in self-similarity may appear when comparing cold events (typically, small earthquakes with low slips and slip rates) with hot events (generally, large earthquakes with high slips and slip-rates) within a given sequence.

If the preferred mechanism for a magnitude-dependent dynamic weakening is fluid pressurization, we expect that only the faults characterized by low gouge and damage zone permeability may develop dynamic lubrication. In this paper we will show six cases in which breaks in self-similarity occur with different severities.

Although in most cases we do not have direct information about fault permeability, valuable borehole and laboratory information is available for the Chelungpu fault, which is responsible for the Chi-Chi earthquake of 20 September 1999 ($M_w$ 7.6). This fault is very important for the seismological community (and for the present study): it represents a specific case in which portions of a fault that cumulate a substantial amount of slip (8-10 m) are at such a shallow depth that they could be reached by borehole, and samples of the fault core could be extracted and analyzed for investigating the energetics of the mainshock (Ma et al., 2006).

Laboratory experiments were performed on different parts of the fault, indicating different permeability structures. Tanikawa and Shimamoto (2009) concluded that the fault is divided in two patches: a southern one with high permeability, and a northern patch with low permeability. Tanikawa and Shimamoto also performed friction experiments and determined that the low-permeability patch to the north is characterized by velocity strengthening frictional properties (i.e., stable sliding) at low slip rates, whereas the southern patch with high permeability is characterized by velocity weakening (i.e., unstable sliding). Based on results from a numerical model, they stated that, during the Chi-Chi mainshock, substantial thermal fluid pressurization occurred on the northern patch of the Chelungpu fault, whereas the more permeable host rocks and core materials of the southern patch did not allow dynamic lubrication.

Tanikawa and Shimamoto provided a lab estimate of dynamic friction coefficients for samples taken on each one of the fault patches: $\mu_d = 0.15$ was obtained for the northern part of the fault, $\mu_d = 0.22$ for the southern part, whereas Kano et al. (2006) determined a very low dynamic friction coefficient on the northern fault patch during the Chi-Chi main shock ($\mu_d = 0.04 \div 0.08$). After considering the large range of possible values for $\mu_d$ on the northern psrt of the Cheungpu fault, we decided that, for our calculations, we would have used a "conservative" estimate, $\mu_d = 0.2$, close to the mean of those given by Tanikawa and Shimamoto (2009).

Based on borehole temperature measurements, the dynamics of faulting of the Chi-Chi event was recently studied by Wang (2009): in order to explain the shear stress-slip function inferred by Ma and Mikumo from seismic data (unpublished manuscript, 2008), he hypothesized the occurrence of severe dynamic weakening through thermal pressurization. In the square patch of the fault that contained the borehole in which the sample of the fault core shown in Wang (2009) was taken, the unpublished shear stress-slip function of Ma and Mikumo showed a strongly decreasing shear stress as a function of slip, reaching a null value at 10.7 m of slip, before going up again to a final shear stress level of 4.6 MPa. In his conclusions, Wang (2009) cited a previous study (Wang, 2008, unpublished manuscript), in which he modeled the coseismic frictional heat of the Chi-Chi mainshock in the same square fault patch, and found that during faulting most of the heat was retained within the slip zone, consistently with the hypothesis of dynamic lubrication by thermal pressurization. Consistently with our findings, he concluded that the seismic radiation efficiency varies very much with the earthquake size for small events, whereas it stays almost constant for large earthquakes.

Because of the amount of information available in the literature on the Chi-Chi mainshock and seismic sequence, and on the Chelungpu fault in particular, our results on this sequence are particularly emphasized in this study. Unfortunately, no specific information on fault architecture and permeability structure, or on fault frictional properties, are available for the rest of the sequences that are investigated here.

This study describes a total of six different mainshock/aftershock sequences: (1) San Giuliano (Southern Italy), (2) Colfiorito (Apennines, Central Italy), (3) Wells (NV), (4) Hector Mine (CA), (5) Chi-Chi (Taiwan), and (6) Iwate (Japan). Results are given in terms of the coefficients of dynamic friction relative to each event in all sequences. We show that dynamic weakening characterizes all the sampled seismic sequences, severely in some cases. Differences in the dynamic behaviors of the studied faults/fault zones are explained in terms of the different effectiveness of thermal pore fluid pressurization due to frictional heating. On each individual fault, the phenomenon is modulated by the permeability of the fault zone.

## Role of fluid pressure in faulting

The role of pore fluid pressure in fault mechanics is extremely important in both static and dynamic conditions: it determines the fault strength during the inter-seismic period, and it may strongly affect the coseismic phase by lubrication effects induced by dynamic pulses (Malagnini et al., 2008). In static conditions, numerous studies are available on the

spatial (generally depth) distribution of pore fluid pressure within the crust, or on temporal fluctuations induced by a spatially and temporally varying bulk permeability, which is controlled mostly by active faulting (Sibson, 1994; Hunt, 1990; Barton et al., 1995; Miller et al. 2004; Townend and Zoback, 2000). Generally, pore fluid pressure in the Earth's crust greatly varies with depth, and so does its gradient. Fluid pressures may be anything between underpressured (Hunt, 1990), hydrostatic and lithostatic. When pore fluid pressure gets too large, it can be relieved through the occurrence of hydrofracturing.
Pore fluids in a crystalline crust are generally in hydrostatic conditions (Zoback and Townend, 2001; Zoback and Townend, 2001; Grawinke and Stockhert, 1997). On the contrary, regions characterized by substantial sedimentation rates may be characterized by buried overpressured compartments, and by super-hydrostatic gradients. High pore fluid pressures are generally found in accretionary prisms (Caine et al., 1996).
Hunt (1990) analyzed the mechanisms of overpressure generation, and the relationships between the nature and distribution of abnormal pore fluid pressures and the presence of oil reservoirs. One of his observations is of our particular interest: the depths of the top seals of the overpressured reservoirs in his worldwide data set cluster around 3000 m.
In deforming sedimentary basins, gradients of pore fluid pressure may turn to lithostatic at the depth where compaction ceases, and below which sediments are increasingly undercompacted and overpressured. Such depth represents the top seal of an overpressured compartment, and may be called fluid retention depth (Suppe and Yue, 2008).
Meeting specific sedimentation/deformation conditions is not the only way to reach crustal fluid pressures in excess of hydrostatic conditions. In some situations (e.g., the Umbria-Marche region of the Colfiorito sequence), the confined fluid (overpressured $CO_2$) is of mantle origin, and percolates upward through the crust until it reaches a seal where a sub-horizontal pressure discontinuity may form. In such a case, the expression "fluid retention depth" is no longer to be used for identifying the top of the overpressured compartment.
However, the mechanical influence of the overpressured fluids on the seismogenic faults is independent of the nature of overpressure, and thus in all cases we will indicate the depth where the transition to a super-hydrostatic pressure regime occurs with the same

general expression (gradient transition depth, $Z_{GT}$, see Figure 1), regardless the nature of the transition itself. For simplicity, in our pore fluid pressure model, we will only deal with hydrostatic and lithostatic gradients. The reader should note that, regardless the "true" pressure-depth profiles, any absolute value of pore fluid pressure at depth can be met by varying the $Z_{GT}$ parameter (Figure 1).

For what concerns our study, direct measurements of pore-fluid pressure at depth are available only for one single point on the Chelungpu fault, where the Chi-Chi main shock occurred. For each one of the analyzed seismic sequences, the available information taken from the scientific literature is listed in the specific subsections of Appendix A1.

**From Seismic Source Scaling to Dynamic Friction**

We show how the uneven scaling of seismological data may be interpreted as the signature of dynamic frictional weakening of earthquake faults, compatibly with observations of laboratory experiments performed on fault rocks. We use recently developed low-noise spectral measurements techniques (Mayeda et al., 2007; Mayeda and Malagnini, 2009), which provide very accurate estimates of radiated energy, in order to investigate details of the physics of faulting which can be related to non self-similar behavior. We compare the estimates of the co-seismic temperature rise to the amount of relative friction drop in six seismic sequences around the world. We show our results in terms of the apparent dynamic friction coefficient $\mu_d$ of the investigated faults, defined as the ratio of dynamic shear stress to effective normal stress:

$$\mu_d = \frac{\tau_d}{\sigma_n - P_f}, \quad (1)$$

where $\tau_d$ is the dynamic shear stress, $\sigma_n$ is the normal pre-stress, and $P_f$ is the pore fluid pressure. By definition of dynamic stress drop $\Delta\tau_d$, we may write:

$$\tau_d = \tau_0 - \Delta\tau_d, \quad (2)$$

where $\tau_0$ is the initial stress. It is easy to show that:

$$\mu_d = \mu_s - \frac{\Delta\tau_d}{\sigma_n - P_f}, \quad (3)$$

where $\mu_s$ is the static coefficient of friction. All quantities are assumed to be an average across the fault, and $\tau_d$, $\mu_d$ are computed for each event. This is a limitation of our method, since faults are highly inhomogeneous and both friction and stress will vary across the fracture surface. In order to compute $\mu_d$ based on equation (3) we require an accurate estimate of the dynamic stress drop, which is the critical parameter expected to vary from event to event in case of frictional weakening. We also require an independent estimate of values, or range of possible values, for the normal stress $\sigma_n$ and the ambient pore pressure $P_f$, and, for equation (2), for the initial shear stress $\tau_0$, as we discuss later on.

We propose a simple relation between dynamic stress drop and radiated energy, based on the energy balance for an expanding crack. The expanding crack model, though it is an idealization and a simplification of the actual faulting process, is physically more reasonable than the Brune model, which assumes an instantaneous stress pulse on the entire fault. Our crack model assumes that the main dynamic friction drop takes place in a small region located in the immediate vicinity of the advancing crack tip; under such conditions it was shown (Freund, 1990) that radiation of seismic energy essentially originates from the vicinity of the crack tip. It can be shown (Appendix A2 to this study) that the dynamic stress drop is proportional to the radiated energy $E_R$ through the equation:

$$\Delta\tau_d = F\ \mu\frac{E_R}{M_0}, \qquad (4)$$

where $\mu$ is the shear stiffness of rocks and $M_0$ is the seismic moment. The proportionality factor $F$ is a dimensionless coefficient (of the order of unity) which, in the crack model, depends essentially on the ratio of fracture speed to wave velocity. However, we expect that the value of $F$ analytically derived for the crack model is an underestimate for natural earthquakes, where radiation is affected by the complexity of the rupture process; we propose instead to estimate a lower bound of $F$ from the seimological data as outlined in Appendix A2.

The quantity $\mu\frac{E_R}{M_0}$ is also known as the apparent stress (Wyss, 1970). The accurate estimate of radiated energy, $E_R$, is obtained through a recently developed spectral ratio method, yielding low variance estimates with respect to classical techniques (Appendices A1.1 through A1.6; Appendix A2; Wyss, 1970).

According to equation (3), the magnitude of dynamic friction scales with the effective normal stress $(\sigma_n - P_f)$, the value of which cannot be precisely known. Moreover, the stress ratio in equation (3) depends upon the orientation of the fault plane with respect to the principal stress axes (the angle $\theta$ indicated in Figure 2), and the final result depends also upon the initial static friction coefficient. It is well known that the absolute level of stress within the Earth is practically impossible to measure, except punctually at borehole sites. Indeed, the value accessible through seismological observations is only the relative co-seismic stress drop (Kanamori and Heaton, 2000), with the remarkable exception of cases where the coseismic rake rotation can be inferred, (Spudich, 1998). As a consequence, we explore a range of different values: results for a limited range of parameters are shown here, and more can be found in Appendix 1. The range of the admissible normal stress $\sigma_n$ and shear pre-stress $\tau_0$ (Figure 2) is estimated by assuming Andersonian faulting and by varying the orientation of faults with unknown orientation, like strike-slip ones, from optimal to unfavorable (Sibson, 1974). Let $\sigma_1, \sigma_2, \sigma_3$ be the maximum, intermediate and minimum effective principal stresses (including the effect of pore pressure $P_f$), with the convention of positive compressive stress; let $\rho_r\, g\, z$ be the lithostatic load. Then Andersonian faulting equates to assuming that one of the three principal stress axes is vertical and that $\sigma_3 = \rho_r\, g\, z - P_f$ for thrust faulting, $\sigma_1 = \rho_r\, g\, z - P_f$ for normal faulting, $(\sigma_1 + \sigma_3)/2 = \rho_r\, g\, z - P_f$ for strike-slip faulting. For optimally oriented faults only, there is a relationship between $\theta$ and $\mu_s$ such that $\theta = 0.5 \arctan(1/\mu_s)$ (Sibson, 1974). However, in the general case of non-optimally oriented faults they are independent and we have to solve for the following system where $\tau_y$ is the yield stress:

$$\begin{cases} \tau_y = \mu_s\, \sigma_n \\ \tau_y = \dfrac{\sigma_1 - \sigma_3}{2} \sin(2\,\theta) \\ \sigma_n = \dfrac{\sigma_1 + \sigma_3}{2} - \dfrac{\sigma_1 - \sigma_3}{2} \cos(2\,\theta) \end{cases} \qquad (4b)$$

Different fluid pressure distribution with depth are tested by varying the fluid gradient transition depth (Suppe and Yue, 2008), $z_{GT}$, according to the following profile:

$$P_f = \begin{cases} \rho_w g z & z \le z_{GT} \\ \rho_w g z_{GT} + \rho_r g (z - z_{GT}) & z > z_{GT} \end{cases} \qquad (5)$$

where $\rho_w$ and $\rho_r$ are the densities of water and rock, respectively (Figure 1).

According to the above definitions, in the case of thrust faulting we obtain:

$$z \le z_{GT} : \begin{cases} \sigma_n = \dfrac{g\, z\, (\rho_r - \rho_w) \cos(\theta)}{\cos(\theta) - \mu_s \sin(\theta)} \\ \tau_y = \mu_s \sigma_n \end{cases} \qquad z > z_{GT} : \begin{cases} \sigma_n = \dfrac{g\, z_{GT}\, (\rho_r - \rho_w) \cos(\theta)}{\cos(\theta) - \mu_s \sin(\theta)} \\ \tau_y = \mu_s \sigma_n \end{cases} \qquad (5b)$$

and equivalent expressions for the case of normal faulting:

$$z \le z_{GT} : \begin{cases} \sigma_n = \dfrac{g\, z\, (\rho_r - \rho_w) \sin(\theta)}{\mu_s \cos(\theta) + \sin(\theta)} \\ \tau_y = \mu_s \sigma_n \end{cases} \qquad z > z_{GT} : \begin{cases} \sigma_n = \dfrac{g\, z_{GT}\, (\rho_r - \rho_w) \sin(\theta)}{\mu_s \cos(\theta) + \sin(\theta)} \\ \tau_y = \mu_s \sigma_n \end{cases} \qquad (5c)$$

and strike slip faulting:

$$z \le z_{GT} : \begin{cases} \sigma_n = \dfrac{g\, z\, (\rho_r - \rho_w) \sin(2\theta)}{\mu_s \cos(2\theta) + \sin(2\theta)} \\ \tau_y = \mu_s \sigma_n \end{cases} \qquad z > z_{GT} : \begin{cases} \sigma_n = \dfrac{g\, z_{GT}\, (\rho_r - \rho_w) \sin(2\theta)}{\mu_s \cos(2\theta) + \sin(2\theta)} \\ \tau_y = \mu_s \sigma_n \end{cases} \qquad (5d)$$

We find that our results are relatively insensitive to fault orientation and static friction coefficient, and that the only relevant parameter for our study, which can be derived from equation (5), is the pressure ratio $\lambda = P_f / \rho_r g z$ at the seismogenic depth.

In the following developments, we shall assume that the difference between initial and yield stress is negligible on the studied faults, i.e., $\tau_y = \tau_0$. While this is a limit case, the more likely situation where $\tau_0 < \tau_y$ equates to lowering the value of the static friction coefficient $\mu_s$ in the model. Since we explore a range of different static friction values (which, as commented above, does not alter the results significantly), we implicitly account for different prestress levels.

The presence of fluids within the fault core at the occurrence of an earthquake is not a necessary condition for dynamic lubrication to occur through fluid pressurization. Experiments on marbles (Han et al. 2007; 2009) and on dolomites from the Colfiorito fault system (De Paola et al., 2008) showed production of $CO_2$ and water as a result of the decomposition of fault rocks induced by shear heating. As a consequence, the dynamic pressurization of the newly produced fluids would induce enough lubrication to sustain possible initial dynamic weakening due to the pressurization of pre-existing ambient fluids, maybe already in super-hydrostatic pressure conditions, and extend the mechanism where overpressurization is not already in place. Moreover, even though nucleation may be more likely to occur in overpressured patches of the fault plane, dynamic pressurization of $CO_2$ from thermal decomposition can either sustain dynamic weakening where ambient pore pressure is low, or boost dynamic lubrication if the dynamic weakening is already driving the rupture.

Finally, we introduce the co-seismic temperature as an indicator of thermally activated lubrication effects on the fault. The thermal diffusion problem (Carslaw and Jaeger, 1959) can be solved by imposing the work rate $V\tau_d$ as a heat source on the fault plane. Assuming constant slip rate $V$ and stress $\tau_d$ during the slip, we obtain the temperature evolution (Nielsen et al., 2008):

$$T = T_i + \frac{2V\tau_d\sqrt{t}}{\rho_r c\sqrt{\pi\kappa}} \qquad (6)$$

$T_i$ is the ambient initial temperature, $t$ is the duration of sliding, $\kappa$ is the heat diffusivity, $\rho_r$ is the rock density, and $c$ is the rock specific heat. Finally, the average dynamic frictional stress $\tau_d$ on the fault is given by equation (2). For seismological applications, $t$ needs to be of the same order of magnitude of the rise time. Under the usual assumption that rupture duration scales with Brune's corner frequency $f_c$, and observing that rise-time appears to last about 10% of rupture duration (Heaton, 1990), we may write $t \cong 1/(10f_c)$. It should be noted that the temperature estimate of equation (6) may not be the actual temperature on the fault plane, but rather an indicative maximum temperature reached in case that no heat was lost in phase transitions (melting, fluid pressurization) or fluid convection. It is, though, representative of the power density produced coseismically per unit fault surface.

## Fault maturity and apparent stress

Choy et al. (2006) used a global data set of shallow-focus earthquakes, and classified the seismogenic faults based on their apparent stress, that is, a measure of the seismic energy radiated by a square meter of fault, in a meter of coseismic slip. They observed that the average of the apparent stress calculated worldwide for subduction earthquakes was the lowest, whereas the average apparent stress of strike-slip events was the highest (most of them were intraplate oceanic earthquakes that ruptured fresh oceanic crust, and the rest were from transform faults). Finally, the average apparent stress calculated on a global data set of normal faulting earthquakes had an intermediate value, on the low side.

Choy's (2006) translated the information on the average apparent stress in terms of fault "smoothness" (i.e., earthquakes generated on "smoother" structures have lower apparent stresses), and thus in terms of fault "maturity", because the faults with larger cumulative offsets are expected to be smoother. In their framework, subduction faults are the most mature structures on earth, whereas the least mature faults are the oceanic transforms that rupture fresh oceanic crust.

In the context of the present study, an immature fault is defined as a structure that accumulated a maximum total amount of slip of the order of a few kilometers only (Shipton et al, 2006), and may be characterized by a thin core and a thin damage zone. For geometrical reasons, if we exclude listric, sub-horizontal detachments which can cumulate large offsets, normal faults cannot accommodate a cumulative offset that is much larger than a fraction of the thickness of the seismogenic zone where they are active, and thus they should be relatively immature. Examples in our data set are Colfiorito and Wells. Even though fault size may not necessarily imply the level of maturity, small strike-slip faults need also to be immature (an example may be the fault responsible of the San Giuliano sequence), whereas Hector Mine is a larger fault characterized by a larger cumulative offset, and it is probably more mature.

On the contrary, a mature fault is a structure that accommodated a cumulative slip up to several tens or even hundreds of kilometers, and that typically possesses a large damage zone. Examples of mature faults, in the sense defined here, are found in subduction zones, where hundreds of km of oceanic lithosphere may slip past the bottom of the more buoyant continental lithosphere, or in mature transform fault zones like the San Andreas, for which Revenaugh and Reasoner (1997) estimated a cumulative offset ranging between 300 and 330 km. Across the San Andreas fault zone, Unsworth et al. (1999) found anomalous low-resistivity zones up to 1 km thick, which were interpreted as volumes permeated by fluid-filled fractures in the wide damage zone.

In the hypothesis that breaks in self-similarity take place beyond a critical magnitude threshold due to fluid pressurization, the characteristics of coseismic flow of pore fluids within the fault zone, and thus the potential for dynamic fluid pressurization during large earthquakes, must be determined by the architecture of the fault zone itself (made of its core and damage zone), via its permeability structure. This is where the fault maturity may come into play.

**Fault permeability structure and dynamic behavior**

Caine et al. (1996) provided a possible classification of faults based on the ratio between the width of the damage zone and the fault zone's total width (damage zone plus fault core), in which the (high) permeability of the damage zone is dominated by its network of fractures, and where the (low) permeability of the fault core (interseismically) is generally less than the permeability of the host rocks. They based their classification on two parameters, thickness of fault core, and total thickness of the fault damage zone. Four end-members may be recognized:

- E1) thin-cored faults with no damage zone;
- E2) thick-cored faults with no damage zone;
- E3) thin-cored faults with a wide damage zone made of thin-cored fractures;
- E4) thick-cored faults with wide damage zone.

The hydrological behavior during the coseismic phase of an E1-type fault is that of a thin conduit, with the ability of becoming a fluid barrier when resealed, shortly after the earthquake. The fluid flow in such a fault takes place through its core, and dynamic fluid pressurization is most likely to occur. We state that E1-type faults may be found in the Apennines, where we observe substantial dynamic effects at the largest magnitudes of our data sets, which we interpret as dynamic lubrication through pore-fluid pressurization.

In Caine et al.'s (1996) classification, accretionary prisms coincide with the E3-type end-member, in which a large fault zone (decollement) is characterized by a thin core, and by a very large damage zone permeated by a network of thin-cored fractures. As a consequence of such architecture, the permeability structure of an accretionary prism is that of a distributed conduit (Moore and Vrolijk, 1992), where the transport of fluids is dominated by fracture flow, and where large dynamic pulses of fluid pressure may still occur.

Accretionary prisms are generally characterized by very high pressures of pore fluids, sometimes close to lithostatic values (Moore and Vrolijk, 1992). In case of the large Chi-Chi earthquake, which occurred on the Chelungpu decollement, there are borehole measurements of super-hydrostatic pressures at depth (Tanikawa et al., 2004). These observations are in sharp contrast with the hydrostatic pressure field predicted by Yue (2007) down to 10 km.

Based on wedge tapers' experiments, Suppe (2007) used Yue's (2007) results in order to compute an extremely low strength for the Chelungpu fault. In any case, whether the pore-fluid pressure is hydrostatic or lithostatic, the Chelungpu detachment may be characterized by low coefficients of static friction. At least, locally.

As far as the dynamic coefficient of friction is concerned, significant dynamic lubrication must have taken place during the Chi-Chi main shock. At least the northern part of the fault, for which Ma et al. (2003) hypothesized the occurrence of substantial elasto-hydrodynamic lubrication that caused a large pulse of ground velocity and low acceleration amplitudes. A substantially different behavior must have characterized the southern portion of the Chelungpu fault, which caused large ground accelerations and low velocity amplitudes (Ma et al., 2003).

In addition to Wang (2009), whose conclusions on the occurrence of dynamic pressurization on the Chelungpu fault during the Chi-Chi earthquake have already been described in a previous section, the same hypothesis was formulated by Ishikawa et al. (2008), on the ground of the analysis of core samples from three active areas of the fault zone, and by Doan et al. (2006), based on the low hydraulic diffusivity observed *in situ*, together with the presence of high-temperature fluids. Their interpretation was that the average stress-drop of the Chi-Chi main shock was dominated by the rupture of the asperity to the south, whereas the northern part of the fault did passively follow the dynamic push. In other words, when pushed beyond a critical slip velocity, thanks to a dramatic lubrication effect through thermal pressurization, the northern patch of the Chelungpu fault could act as an efficient decoupling interface for the hanging wall. As a consequence of the described dynamics, the northern part of the Chelungpu fault is characterized by aftershocks with low values of apparent stress, whereas the large values of the aftershocks' apparent stresses are all concentrated in the southern side of the fault zone, as shown in Figure A9.

Finally, two recent works went down to the root of the problem of the complex seismic radiation observed during the Chi-Chi main shock: the first one (Tanikawa and Shimamoto, 2009) provided estimates of the permeability coefficients in the northern and in the southern patches of the fault, whereas the second one (Noda and Lapusta, 2009, personal communication) used them in order to implement a 3D earthquake model. These two studies allowed us to understand the average behavior of the Chi-Chi sequence, in terms of the observed break in self-similarity, and of the calculated coefficients of dynamic friction.

## Coefficients of dynamic friction

We present the coefficients of friction for the events of six different mainshock/aftershock sequences: (1) San Giuliano (Italy), (2) Colfiorito (Italy), (3) Wells (NV), (4) Hector Mine (CA), (5) Chi-Chi (Taiwan), and (6) Iwate (Japan). All the details of the calculations, together with the descriptions of the sequences and data sets, are left in Appendices A1.1 through A1.6.

Sequences (1) through (3) (Appendices A1.1 through A1.3) occurred on small faults, capable of events with a maximum magnitude between Mw 5 and Mw 6, and Figure 3 shows they are characterized by severe progressive weakening with increasing temperature. Sequence (4) (Appendix A1.4) occurred on a relatively large strike-slip fault. Sequence (5) (Appendix A1.5), occurred on a large structure capable of an Mw 7.6 mainshock, shows very similar apparent stresses between the mainshock and some of the largest aftershocks, but the smaller events have substantially smaller apparent stresses. Sequence (6) (Appendix A1.6) occurred on a crustal thrust fault, ~100 km above a subducting slab: although self-similarity clearly breaks in this data set (see Figures A11 and A12), the computed friction coefficients do not show a dramatic weakening. The different behavior is due to the fact that, for fixed pore fluid pressure, coefficient of static friction, and $\theta$, a thrust fault is characterized by the largest pre-stresses of all the three fault types, and thus by the lowest stress drop/pre-stress ratio, according to equations (2) and (3).

Sequences (4) and (6) occurred on structures capable of $M_w$~7 mainshocks. They both show that below $M_w$~5.5, the aftershock sequences look self-similar, but a jump in the apparent stresses is necessary to match the mainshocks. A similar behavior, although more complex, distinguishes sequence (5), occurred on the Chelungpu fault, which is capable of $M_w$ 7.6 earthquakes. Even though we know the importance of the maximum magnitude that can occur on each structure, we stress that the relationship between $M_{wMAX}$ and fault maturity is anything but simple.

In the results of Figure 3, we note that the amount of absolute fault weakening (i.e., the value taken by the coefficient of dynamic friction, $\mu_d$) does not depend only on how far the sequence is from self-similarity: Appendix A2 demonstrates that the absolute value of $\mu_d$ depends on: 1) the fault type (thrust, normal, or strike-slip), that is, on the prestress level, 2) the orientation of the fault plane with respect to the principal compressional stresses, and 3) (as seen in Figure 3) on the ambient pore fluid pressure. Of all sequences shown in this study, regardless its substantial departure from self-similarity (Figures A11 and A12), sequence (6) seems to be characterized by the least "absolute" dynamic weakening.

## Discussion

Possible causes of bias in the results should be carefully checked, in particular, the eventuality of an insufficient bandwidth in the measurements concerning smaller events (Bill Ellsworth, personal communication, 2008). Indeed, calculations based on data with limited bandwidth in the high-frequency range would neglect a large part of the seismic energy radiated by smaller earthquakes, thus biasing their dynamic stress drops toward lesser values. In this case the observed source scaling of Figure 3 would be an artifact and may not allow to conclude against self-similarity. We verified that for results of Figure 3, A1, A3, A5, A7, A9, and A11, the bandwidth does include the corner frequencies of the smaller events. Further evidence is provided in the Figures A2, A4, A6, A8, A10, and A12, where the observed spectral ratios (red squares) and the theoretical best fit curves are shown (solid blue sigmoidal curves). In each figure, the horizontal blue solid lines represents the theoretical asymptotic low- and high-frequency limits of the spectral ratio for two perfectly self-similar earthquakes. The low-frequency limit of $M_{01}/M_{02}$ (where $M_{01} > M_{02}$) is represented by the top horizontal, solid blue line. The high-frequency limit of $\left(M_{01}/M_{02}\right)^{1-\frac{p}{3}}$, where $p$ is the high-frequency roll-off parameter of the observed spectra (in the specific case where $p = 2$), is represented bottom horizontal, solid blue line.

We observe that dynamic weakening, when present, is always strongly correlated with earthquake magnitude (Figure 4). Nevertheless, in order to stress the existence of some thermally-activated processes, the coefficients of dynamic friction given by equation (3) are always shown as a function of the virtual fault temperature computed using equation (6).

Figure 5 goes down to the core of our results: the apparent stresses calculated for all events, in all sequences. The most important attribute of our measurements is represented by their extreme accuracy, which could be reached only by using the coda-based methodology initially developed by Mayeda et al. (2007), and subsequently refined by Mayeda and Malagnini (2009). Based on the $\left(M_0, \sigma_a\right)$ pairs of Figure 5, and on information on fault orientation taken from the published moment tensor solutions (dip-slip faults), or for three possible orientations for strike-slip faults, we calculated all the dynamic parameters shown in this study.

Figure 5 indicates that non-self-similar source scaling characterizes all sequences: the logarithm of the apparent stress tends to increase linearly with the logarithm of the seismic moment, at least up to a moment magnitude $M_w$ between 4.5 and 5.5 (the Iwate data set seems to be an exception to the rule), and saturates to a constant value beyond a threshold moment magnitude, between $M_w6$ and $M_w7$. A limiting value for the apparent stress, well below 10 MPa, is common to all sequences.

For a given fault zone, the process of dynamic weakening is indicated by the temperature dependence of the coefficient of dynamic friction, which generally decreases when the fault temperature increases coseismically. The invoked physical mechanism is that of the abrupt buildup of thermal fluid pressurization within the fault core during slip. For the sequences analyzed, we hypothesize that substantial weakening is likely to occur on the thin-cored end-members (E1, E3) of the classification scheme of fault zones provided by Caine et al. (1996).

In particular, the analysis of the Chi-Chi sequence shows that dynamic weakening may occur regardless of the presence of a wide damage zone, if the latter is made of a network of fractures that still allows dynamic pressurization to occur on the main fault. In such an environment, in order to maintain the super-hydrostatic pore fluid pressure that is observed inter-seismically in boreholes above the Chelungpu fault (Tanikawa et al., 2004), the same network of fractures need to be effectively sealed, at least during the inter-seismic periods.

We hypothesize that the presence of pore fluids always tends to prevent excessive temperature increases. On faults where fluid confinement is not efficient due to a core and damage zone of high permeability, heat may be removed from the fault core by fluid advection. On the contrary, on faults where confinement is efficient, the thermal response of pore fluids to frictional heating allows lubrication by core pressurization. The effect of fluid pressurization as a function of increasing temperature may be understood by looking at the different families of dynamic friction coefficients plotted in Figure 3, or at the complete set of plots shown in Figures A1, A3 A5, A7, A9, and A11. Our qualitative argument is that both mechanisms (dynamic lubrication or fluid flow) will tend to prevent, or limit, melt production and temperature rise. In the scarcity of fluids, we expect lubrication to occur through melting, decarbonation, gel formation, or any lubrication mechanism other than fluid pressurization, as discussed in the Introduction.

All events analyzed in this study are assumed to occur on the mainshock's fault plane, which is most probably the case at least for the largest aftershocks. However, one can argue that the small aftershocks of some sequences may occur, within the location error, either on the main fault plane, or on off-plane fractures driven by the local (residual) stress fields (Mayeda and Malagnini, 2009). Regardless of their locations, our calculations show that the small earthquakes in our sequences never dissipate enough frictional energy to thermally pressurize pore fluids. As a consequence, the information of whether the small aftershocks are located on or off the main plane is irrelevant to our conclusions. In other words, the positions of the small events in the plots of dynamic friction vs. temperature of Figure 3 are always in the upper left corners of the different frames, and would not appreciably change if we had to use slightly different fault orientations.

## Conclusions

Based on the results shown in Figure 3, and on the details of the analyses described in Appendices A1.1 through A1.6, we conclude that pore fluid pressurization, as a physical mechanism for causing fault weakening, is compatible with the departure from self-similarity observed in the discussed seismic sequences. Such phenomenon is effective only if fluids remain trapped in narrow vessels. Alternatively, if pore fluids are allowed to expand in wider regions of high permeability around the fault core, they can remove heat from the primary slip zones by advection rather than pressurizing the fault. In either case (lubrication or heat removal), the presence of fluids is expected to limit the coseismic increase of fault temperature.

In the hypothesis that fluid pressurization is the key mechanism, a fault classification based on maturity may not be able to capture the average dynamic behavior of all the different structures. More suitable for this task would be a classification scheme based on the permeability architecture of the fault core and damage zone (Caine et al., 1996), for which the opposite end-members, from most prone to dynamic lubrication, to least prone to dynamic lubrication, are:

- E1, E3) thin-cored faults, with or without a wide damage zone of thin-cored fractures, respectively. In our interpretation, dramatic dynamic lubrication is likely to occur on these faults/fault zones, and we show evidence that, within a specific sequence occurred on such structures, the average dynamic friction is indeed smaller for larger and hotter events.
- E2, E4) thick-cored faults with or without a wide damage zone, respectively, for which we imagine the volumes containing the primary slip zones pervasively crisscrossed by permeable networks of fractures. Faults like these are more likely to behave self-similarly, unless/until other weakening mechanisms, like melt production, would take over. We believe we do not have examples of such end-members in the investigated data sets.

Small, immature faults may not have wide damage zones, and thus they probably are E1-type. On the contrary, for a mature fault like the San Andreas, the damage zone may be up to ~1 km-wide (Shipton et al., 2006), and the permeability structure of a wide damage zone may, in specific cases, prevent fluid and heat containment during faulting. In the Caine's classification, accretionary prisms like Taiwan are the prototypes of the thin-core-wide damage-zone end-member that we named E3.

Based on our results, we think that the two fault classification schemes (the one based on maturity, and the one based on permeability structure) need to partially overlap, but it must be the permeability structure of a fault what dominates its behavior. Our hypothesis is that immature faults with very small cumulative slips are likely to be E1-type structures (sequences (1), (2), and (3)), whereas the Chelungpu fault (sequence (5), by definition an E3-type fault zone) is probably a smoother, more mature, structure. Yue et al. (2005) found that the Chelungpu fault accommodated a total displacement of ~14 km, but the largest slip (~10 m) occurred on a newly propagated (cumulative offset of only 300 m) North Chelungpu Chinshui detachment, which shows abnormally smooth rupture dynamics.

About the Hector Mine and Iwate sequences ((4) and (6)), we believe they may be representative of an intermediate situation in which the fluid pressurization is modulated by a critical value of the permeability of the fault core and damage zone: high enough to dissipate the pressure pulses of the small events but low enough to allow some dynamic lubrication for a large event like the mainshock. About sequences (4) and (6), for which the dynamic weakening is less pronounced, it is interesting to note that they both show a clear non self-similar energy scaling.

Opposite end-members in the maturity classification scheme given by Choy et al. (2006), from less mature to most mature fault zones, are oceanic transform faults that rupture fresh oceanic crust, and subduction faults. For what has been shown in this study, we think it would be important to perform our analysis also on fault maturity end-members. Unfortunately, no complete data sets of broadband waveforms from such kinds of sequences are available at the moment. The analysis proposed here is difficult to apply to subduction events because the distances involved are generally too large to record broadband seismograms of the small events with good S/N ratio, which are necessary for defining the source scaling. For the same reason, data from the other end-members of fault maturity (oceanic transforms on fresh oceanic crust) are also difficult to obtain, and dedicated experiments need to be planned.

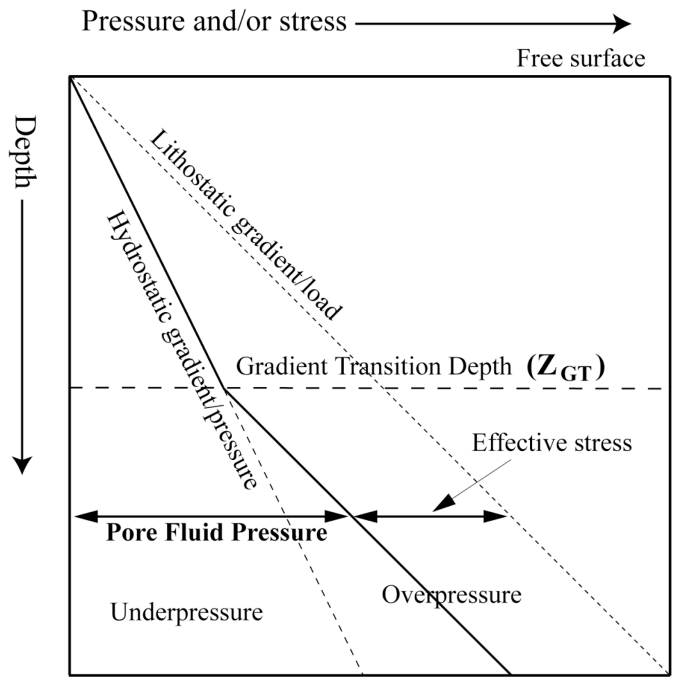


**Figure 1.** Pore fluid pressure vs. depth. We use two possible gradients only, hydrostatic and lithostatic, connected by a variable crossover depth.

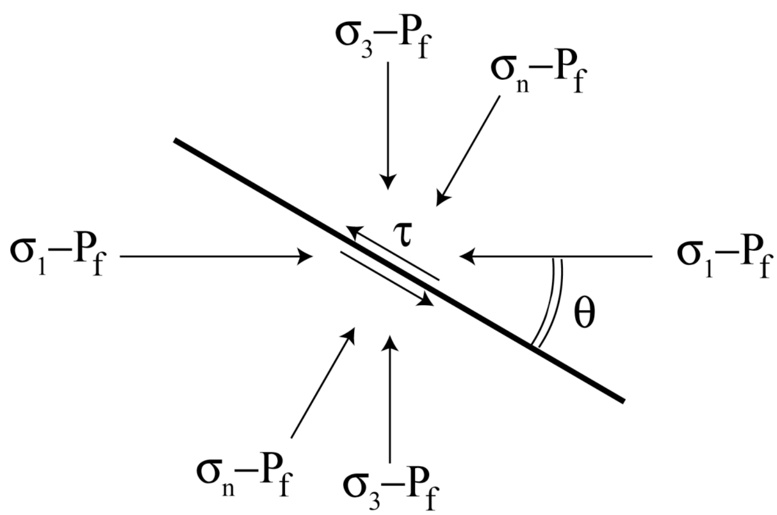


**Figure 2.** Orientation of the maximum and minimum stress axes with respect to the fault plane. The cartoon indicates the conventional relationship used for the angle $\theta$ in the fault geometry. A reverse fault is presented here.

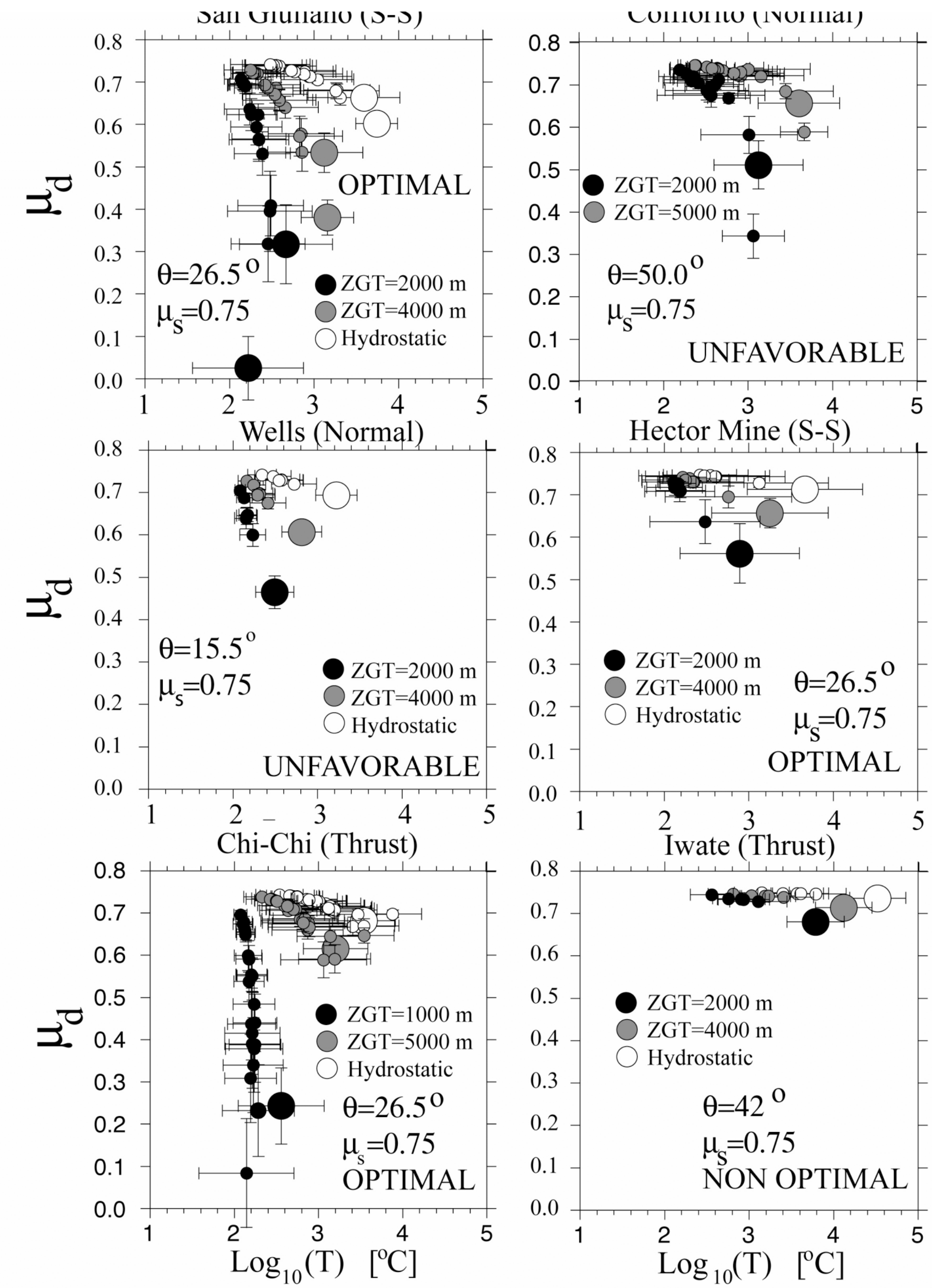


**Figure 3.** Coefficients of dynamic friction computed for the events of the five seismic sequences analyzed in this paper. Shown here is a single calculation for each sequence, but a limited search in the parameter space is given, for each sequence, in Appendix 1. Pressure increases from the white symbols to the black ones, given the corresponding decrease of the fluid retention depth. In other words, for each sequence we fix the pore fluid pressure to three plausible values, and obtain three different "families" of possible friction coefficients: white are hydrostatic conditions, gray are higher pressure, black are very high pore fluid prssures. Larger symbols indicate the mainshock of the specific sequence. For San Giuliano, the figure contains the indication of its two mainshocks.

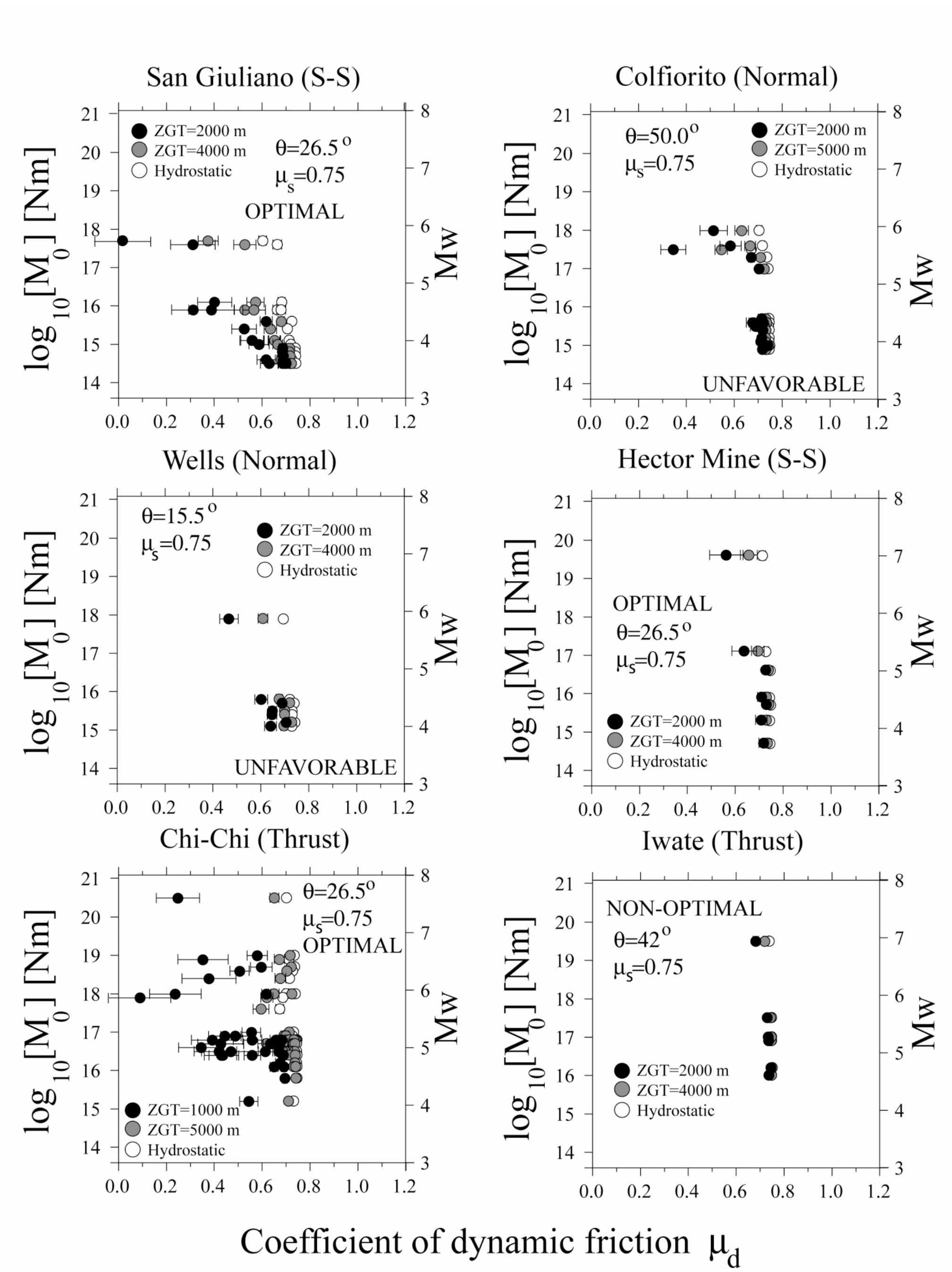


**Figure 4.** The coefficients of dynamic friction shown in Figure 3 are shown here as a function of seismic moment. The picture indicates that, generally, the dynamic friction is strongly correlated with the size of the earthquake. Two apparent discrepancies are observed: 1) the Colfiorito seismic sequence is characterized by multiple mainshocks with comparable size, and the lowest dynamic friction is computed for the second largest event; 2) for the Chi-Chi sequence, the map in Figure A9 indicates that the event with the largest apparent stress (and thus the lower dynamic friction) is not the mainshock, but the largest event occurred within the southern patch of the fault. For the meaning of the gray scale, see the caption of Figure 4.

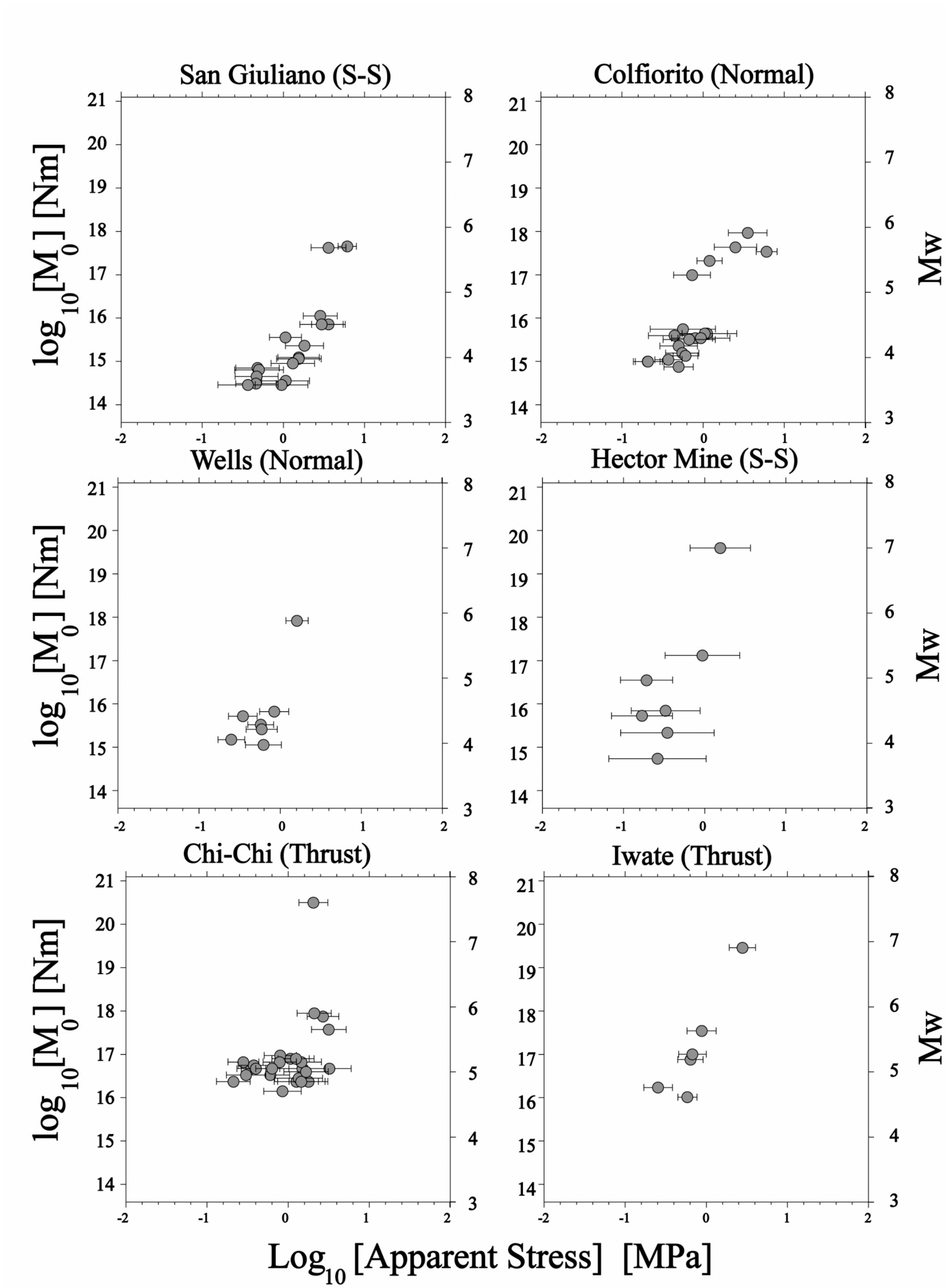


**Figure 5.** Apparent stress (horizontal axes) as a function of seismic moment (or moment magnitude), for the events of the investigated sequences. In each frame, seismic moment is on the left vertical axis, and the corresponding moment magnitude is on the right vertical axis. All sequences are characterized by non-self-similar source scaling.

# Appendices

**Table of contents:**

A1: Details on the analysis of the earthquake sequences

*A1.1: The San Giuliano sequence (Southern Italy)*

*A1.2: The Colfiorito sequence (Central Italy)*

*A1.3: The Wells sequence (NV)*

*A1.4: The Hector Mine sequence (CA)*

*A1.5: The Chi-Chi sequence (Taiwan)*

*A1.6: The Iwate sequence (Japan)*

A2: Scaling of dynamic stress drop with radiated energy

## A1: Details on the analysis of the earthquake sequences

### *A1.1: The San Giuliano sequence (Southern Italy)*

Two mainshocks of similar magnitude ($M_w \sim 5.7$) struck the town of San Giuliano di Puglia (Molise, Southern Italy) on 10/31/2002 at 10:33 UTC, and on 11/01/2002, at 15:09 UTC. The first earthquake caused the collapse of an elementary school, and the death of 26 children and one teacher. Both events had almost pure strike-slip mechanisms, and best centroid depths at 15 km (Catalog of the INGV-Harvard Regional Centroid-Moment Tensor Solutions, http://www.ingv.it/seismoglo/RCMT).

Both the high-quality hypocentral depths of the two mainshocks were below 20 km; the distribution of the aftershocks delineated a single, E-W-striking fault plane, where both mainshocks were located. All the events in the sequence were deeper than 10 km, and the energy radiated by both mainshocks was entirely generated no deeper than 24 km (Latorre et al., 2008).

Breakout data in the adjacent Gargano area demonstrated that the regional stress field is characterized by a horizontal, NE-SW-striking minimum principal stress (Montone et al., 1999), so that the fault orientation, in Sibson's classification (Sibson, 1990), is presumably at the transition between *favorable* and *unfavorable* (i.e., at about $15^0$ from the *optimal* orientation).

In our calculation of shear friction on the fault plane for the events of this sequence (Figure A1), we sample the case where the fault plane is oriented close to the *optimal* reactivation angles, $\theta_r^* = 0.5\tan^{-1}(1/\mu_s)$ (26.5 and 30.0 degrees, for $\mu_s = 0.75$ and $\mu_s = 0.58$, respectively). We also sample *non-optimal orien*tations (5 degrees added to the optimal angles), and *unfavorable orientations* (20 degrees added to the optimal angles). The same orientations are explored for the other strike-slip fault described in this study: the one of the Hector Mine earthquake. Results are based on the best fits shown in Figure A2.

High pore fluid pressure at mid-crustal depths was hypothesized in the region, due to substantial $CO_2$ degassing of mantle origin, and a lower bound estimate for the overpressure parameter ($\lambda = 0.65$) is available at the seismogenic depth (Boncio, 2008; Chiodini et al., 2004). It is not clear at what depth the pore fluid pressure becomes super-hydrostatic, so we produce an exploration of the possible regimes (2000 m and 4000 m for the transition depth, and hydrostatic conditions for comparison). The apparently low stress drop for the San Giuliano mainshocks, and the anomalous pore fluid pressure at depth were erroneously linked together (Boncio, 2008), whereas it was demonstrated (Malagnini and Mayeda, 2008) that both the two main earthquakes have in fact high stress drops: a characteristic to be expected when substantial dynamic weakening is inferred.

Based on the hypothesis of total stress release for the largest mainshock of the sequence, in a regime of high pore fluid pressure (i.e., transition depth set to 2000 m) and optimal orientation to the regional stress field, the coefficient F in equation (36) of Appendix A2 was calibrated to the value F=3.0. That of a null frictional stress is a rather arbitrary choice, although necessary to fix the value of the coefficient F. If we had independent information on the actual value of the dynamic friction, the null friction should have been substituted with the specific value.

The value F=3.0 was used throughout this study, for all the calculations shown. In terms of dynamic behavior, we note that the friction coefficients in Figure A1 define a distribution that systematically decreases with increasing magnitude (or, which is the same, any increase of friction-induced virtual temperature). The cited value for the coefficient F=3.0 represents an upper bound for the conditions described above.

Such behavior indicates a high sensitivity of the dynamic friction to changes in the generated frictional heat, and thus a very efficient confinement of heat and fluids within the fault core during faulting. The described dynamic characteristics of the San Giuliano fault are consistent with the E1 end-member in the Caine (1996) classification (thin conduit/core, no damage zone).

*A1.2: The Colfiorito sequence (Central Italy)*

The first two mainshocks of a long sequence (Amato et al., 1998) occurred in Central Italy on September 26, 1997, at 00:33 UTC, and at 09:40 UTC. A total of six mainshocks with magnitudes Mw between 5 and 6 struck over a time span of about one month. The seismogenic structure consisted of a low-angle extensional fault elongated in the NW-SE direction (dip of about 40º). The extension took place over a reactivated thrust that could be classified at the transition between *favorable* and *unfavorable* orientations (Sibson, 1990). The seismicity of the sequence was confined to the top 8 km of the crust.

The fault-valve behavior of the main fault (Sibson, 1992a,b) was documented during this seismic sequence (Miller et al., 2004): the fault ruptured a seal at a depth of about 5000 m, liberating a large amount of $CO_2$ of mantle origin that was overpressured below this surface (Chiodini et al., 2004). The present study analyzes six spectral ratios, computed between two of the maishocks ($M_w$ 5.91 and $M_w$ 5.48), and five aftershocks with coda magnitude $M_w$ between 3.85 and 4.29. The depth of the top of the pressured volume in the area was fixed to 5000 m: due to the shallow depths of the earthquakes, hydrostatic conditions would yield overlapping results with those of a seal depth of 5000 m. For comparison, results for a seal depth of 2000 m are also computed. Results are shown in Figures A3 and A4.

It is well known (Sibson, 1994) that fault-valve behaviors may modulate the regime of the pore fluid pressure in the entire crust, and thus the events that occurred later in the sequence may have experienced a substantially lower pore fluid pressure with respect to those occurred at its beginning. The amplitude of the described variation in the pore fluid pressure within the sequence was neglected in our calculations.

Dynamic weakening by fluid pressurization has been invoked by Malagnini et al. (2008) in order to explain the source scaling relationship found for the Colfiorito sequence, for which they found: $M_0 \propto f_c^{-(4.7\pm0.3)}$. The computed dynamic weakening does not seem to correlate with the time elapsed from the mainshock, and thus with the decreasing ambient pore fluid pressure below the broken seal, but a clear correlation is seen with the events' magnitudes.

The pulse of pore fluid pressure experienced above the broken seal triggered some of the aftershocks that entered in our analysis. Our interpretation is that the variations of pore fluid pressure due to the fault-valve behavior is not the dominant mechanism in reducing the dynamic coefficient of friction, at least in the Colfiorito area, but lubrication of immature fault is dominated by dynamic fault pressurization.

Again, for a possible classification of the Colfiorito fault system in Caine's (1996) terms, we can only infer its permeability structure from the observation that the dynamic behavior of the sequence, as described in Figure A3, is very similar to that of the events on the fault responsible for the San Giuliano events. For this reason, we believe that the Colfiorito fault system is close to the E1 end-member of Caine's (1996) scheme.

*A1.3: The Wells sequence (NV)*

On 2008 February 21, at 14:16:02 UTC, the area surrounding Wells (NV) was struck by an Mw 6.0 earthquake. The event occurred during the deployment of USArray in the region. For this earthquake, UC Berkeley computed a normal faulting mechanism, with a slight oblique component. For the epicentral area, the USGS Quaternary Faults and Folds Database indicate the existence of a network of widely distributed faults west of Wells Peak. Nevertheless, based on the revised location, the aftershocks' distribution, and the depth of the mainshock, it was difficult to associate the Wells event with a specific fault (http://earthquake.usgs.gov/eqcenter/recenteqsww/Quakes/us2008nsa9.php#summary). The conjugate planes of the UC Berkeley mechanism dip at 65 and 31 degrees (~32.5 and ~15.5 degrees from the vertical maximum stress, respectively): the first plane is around the optimal orientation to the axis of maximum compressional stress; the second plane is at the transition to the range classified as *unfavorably oriented* (Sibson, 1990).

We analyze 6 spectral ratios, computed between the mainshock (coda-based moment magnitude Mw 5.90), and 6 aftershocks (coda-based moment magnitudes Mw's between 4.10 and 4.57). Results are shown in Figures A5 and A6.

The pore fluid pressure regime in this area is, to our knowledge, unknown, and so a full exploration is performed over standard pressure conditions (overpressure regime with hydrostatic/lithostatic gradient transition at depths of 2000 m and 4000 m, and fully hydrostatic regime), for the two possible orientations of the fault planes. The qualitative analysis of the dynamic behavior of the sequence suggests a low-permeability structure that allows the occurrence of strong coseismic pulses of pore fluids. Although not as extreme as the San Giuliano seismic sequence, we can attribute to this sequence a behavior compatible with that of the end-member E1 in the Caine's (1996) scheme.

*A1.4: The Hector Mine sequence (CA)*

The Hector Mine earthquake, $M_w$ 7.0 (from full waveform inversion, Ichinose, personal communication, 2006), occurred in the Mojave desert on 16 October, 1999, at 09:46 UTC. The focal solution indicated a sub-vertical strike-slip earthquake occurred on a N-NW-striking fault.

The six spectral ratios analyzed in this study were computed between the $M_w$7.0 mainshock and six aftershocks with coda-based moment magnitudes $M_w$'s between 3.76 and 4.97 (Mayeda et al., 2007). Our calculations (Figure A7) are carried out using the same orientations and static coefficients of friction that are used for the San Giuliano sequence (26.5, 31.5 and 46.5 degrees for $\mu_s = 0.75$, and 30.0, 35.0, and 50.0 degrees for $\mu_s = 0.58$, corresponding to optimal, non-optimal, and unfavorable orientation, respectively, for the two coefficients of static friction). The theoretical fits of the observed spectral ratios used for the computation of the results shown in Figure A7 are plotted in Figure A8.

We have no specific data on the pressure gradients in the area surrounding the fault: the only information we have to date (Peltzer et al., 1996) hypothesized hydrostatic pore fluid pressure conditions for the Landers earthquake, whose epicenter lies some 45 km from the Hector Mine epicenter (rupture planes lie about 20 km apart).

Strike-slip faults are not clearly oriented with respect to the axis of the regional maximum compressive stress; an outstanding example in California is that of a major fault like the San Andreas, for which a number of studies invoked the presence of overpressured fluids (or other weakening mechanisms) in order to explain the slipping of a fault that may be, in Sibson's (1990) classification, severely misoriented. In a severely misoriented fault, the reactivation angle (i.e., angle between the fault plane and the maximum compressive stress) is beyond lockup ($\theta_r > 2\theta_r^*$, where $\theta_r^*$ is the optimal reactivation angle). Such faults are able to slip only if the pore fluid pressure is super-lithostatic (i.e., in a strike-slip or reverse-slip fault, $P_f > \sigma_3$), so that the effective stress becomes tensile. Of course, in super-lithostatic pressure conditions, in order for a severely misoriented fault to move, the following condition for the differential stress must be met: $(\sigma_1 - \sigma_3) < 4T$, where $T$ is the tensile rock strength (Sibson, 1990). For higher values of the differential stress, rocks would rupture on a new shear plane at the optimal orientation (or on an existing surface of weakness with a better orientation). In this study we do not sample severely misoriented angles.

The tendency of other California sites towards lithostatic pore pressure conditions was documented based on the analysis of pore fluid pressure measurements from the sedimentary basins within the San Andreas fault system (Sibson, 1990). Since we do not have precise information about the specific area surrounding the Hector Mine epicenter, we will explore the situations where pore fluid pressure around the fault is hydrostatic, or if there is a fluid seal of some sort at depth that allows the build-up of a super-hydrostatic pore fluid pressure, with a hydrostatic/lithostatic gradient transition at depths of 2000 and 4000 m, and for totally hydrostatic conditions as well.

The Hector Mine seismic sequence shows a dynamic behavior characterized by a substantial, yet moderate, decrease of the dynamic friction coefficient only for the mainshock. We interpret such behavior as follows: the permeability of this fault is high enough to prevent substantial lubrication episodes during the small events, but low enough to still allow large pressure pulses to cause dynamic lubrication, at least for M~7 events like the recorded mainshock. A critical slip velocity must exist, above which lubrication takes place, according to the interpretation of a step-like break in self-similarity given for this fault by Mayeda and Malagnini (2007), who predicted the critical cross-over magnitude be $M_w$~5.5. In the Caine's scheme, the Hector Mine fault must occupy an intermediate location, somewhere between the end-members where dynamic pressure pulses can easily occur, and the ones where pressure pulses are forbidden.

*A1.5: The Chi-Chi sequence (Taiwan)*

The Chi-Chi earthquake (Mw 7.6) struck Taiwan on September 20 1999, at 17:47 UTC. The Harvard CMT solution showed a reverse fault mechanism with one of the conjugate planes dipping $25^0$, close to the optimal reactivation angle. The mainshock ruptured the newly propagated North Chelungpu Detachment, and was characterized by an anomalously smooth rupture dynamics (Yue et al., 2005). The peculiar characteristics of the recorded ground motion (large pulse of ground velocity and low accelerations to the North; low ground velocities and large accelerations to the South) make this sequence particularly interesting.

The data set analyzed here is made of 17 spectral ratios calculated between the mainshock and 17 aftershocks with magnitudes ranging between Mw 4.70 and Mw 6.30. Results are displayed in Figure A9, and the best fits are shown in Figure A10. More information on the present Chi-Chi database of spectral ratios is available in the literature (Mayeda and Malagnini, 2009). The $M_0$ vs. $f_c$ plot for this sequence shows a moderate, step-like, departure from self-similarity at Mw ~ 5.5 (lower-left frame of Figure A9).

Taiwan serpentinites (present along the detachments) have been used in lab experiments to explain the extreme dynamic weakening of some faults in terms of the effects of serpentine dehydration, through the subsequent fluid pressurization of the fault core (Hirose and Bystricky, 2007). Such a mechanism could help explain the lack of pronounced heat flow observed along major crustal faults such as the San Andreas (e.g., Brune et al., 1969), and the low temperature anomaly recorded in a borehole that went through a shallow part of the northern patch of the Chelungpu fault (1100 m deep), even six years after the Chi-Chi earthquake.

The latter observation (Kano et al., 2006) is evidence of a very low level of friction that could not generate much heat at the time of the earthquake. From a measured peak value of 0.06 $^0$C for the thermal anomaly observed during the experiments across the northern patch of the Chelungpu fault, with a spatial width of the anomaly of about 40 m (20 m from each side of the peak), a diffusion equation was used in order to estimate a coseismic shear stress of 1.1 MPa, at a depth of 1111 m (Kano et al., 2006). Based on the mentioned observations, conduction must be the predominant mechanism of heat transport in the investigated fault patch, so that the heat transported by fluid flow does not have a dominant effect. This must be true also for the coseismic phase, although the very shallow depth at which the measurements were taken did not assure the sampling of the seismogenic portion of the fault. For the northern patch of the Chelungpu fault, where the temperature anomaly was observed, based on the computed frictional heat, an extremely low apparent coefficient of dynamic friction was estimated by Kano et al. (2006), in the range between 0.04 and 0.08.

There seems to be no unanimous consensus on the pore fluid pressure regime in this region, although an overwhelming portion of the published studies leans toward an over-pressurized environment. Accretionary wedges are generally characterized by pressured compartments (Hunt, 1990): in the region of Tiehchanshan (Taiwan), the seal of an overpressured compartment is found at a depth of about 3200 m (Hunt, 1990).

Nevertheless, hydrostatic pore fluid pressures were predicted by Yue (2007) down to 10 km in the region of the Chi-Chi earthquake (Mw 7.6), and used for the calculation of a very low friction coefficient on the basal detachment of the western Taiwan wedge (Suppe, 2007), that was explained in terms of the presence of weak minerals. Yue's (2007) results conflict with the actual pore fluid pressure measurements taken down a deep borehole reaching the Chelungpu fault in the Taiwan Western Foothills, right in the focal area of the 1999 Chi-Chi earthquake. Such data set showed a clear departure from the hydrostatic gradient 5500 m down a borehole (Tanikawa et al., 2004). Finally, the presence of overpressured fluid compartments in the Hsinchu basin (Hunt, 1990), suggests that such situation may be widespread in the Taiwan accretionary prism.

Tanikawa and Shimamoto (2009) carried out low- and high-velocity friction tests on rock samples from shallow boreholes in the Chelungpu fault, together with measurements of permeability. They showed that the northern part of the fault is characterized by a velocity-strengthening behavior at low velocities, and has very low values of permeability, so that the slip zone is very susceptible of dynamic fluid pressurization when a large rupture, nucleated in the south, is able to push the northern patch past its critical slip velocity, so that the patch may become unstable and a large rupture may occur.

Tanikawa and Shimamoto (2009) showed that, on the contrary, the southern part of the fault is characterized by a velocity-weakening frictional behavior, and by larger values of permeability that inhibit fluid pressurization. Noda and Lapusta (2009), motivated by the laboratory measurements of Tanimawa and Shimamoto (2009), implemented a 3D earthquake sequence simulations for a simplified model of the Chelungpu fault. The model was made of two different patches with different physical characteristics: velocity-strengthening friction and low permeability for the northern patch; velocity-weakening friction and high-permeability for the southern patch. Clearly, events could nucleate only in the southern portion of the fault, but they could propagate also in the northern portion. Generally, stable sliding conditions in the northern patch of the fault killed the rupture propagation, but sometimes, when the slip velocity in the northern patch could go beyond a critical threshold and initiate thermal pressurization, a large event could rupture the entire fault. Noda and Lapusta (2009, personal communication) observed that the combined effect of rate hardening at slow slip rates, and efficient thermal pressurization at high slip rates in the northern patch of the fault is very consistent with the characteristics of the ground motion that were observed during the Chi-Chi earthquake: low accelerations/high velocities/large slips to the north, and high accelerations/low velocities to the south.

The described dynamic interaction between the two main parts of the fault makes the Chelungpu earthquake cycle consist of multiple events of different sizes. The patch to the south, where unstable sliding occurs and dynamic pressurization is forbidden, breaks frequently in smaller events that cannot relieve large amount of shear stress. The region to the north, of more efficient thermal pressurization, produces larger slip when it is ruptured, and thus has lower inter-seismic values of shear stress and does not rupture in every event.

It must be clear that our observations cannot discriminate between the different behaviors of the two fault patches. In fact, our coefficients of friction, plotted in the upper frames of Figure A9, represent a weighted average (on the amount of radiated energy) of the two different behaviors. If, as we hypothesize, the break in self-similarity that affects the main shock was due to dynamic fluid pressurization, the overall effect was lessened by the (more self-similar) contribution of the unstable southern patch. From the visual inspection of Figure A10, the break in self-similarity is very clear.

As for the Caine's (1996) classification, the Chelungpu belongs to the Taiwanese accretionary prism, and thus it is, by definition, an E3 end-member. The northern patch of the Chelungpu fault zone is thus part of a mature detachment where very strong frictional heating-generated pulses of pore fluid pressure are very likely to happen, and where extreme dynamic lubrication may take place. On the contrary, dynamic pressure pulses appear to be forbidden on the southern patch of the Chelungpu fault zone.

As stated in the main text, the fault maturity seems to be too vague in order to be the fundamental characteristics for dynamic lubrication to occur through pore fluid pressurization. For what concerns the Chi-Chi event, however, it is worth repeating that Yue et al. (2005) found that, although the Chelungpu fault accommodated a total displacement of ~14 km, the largest slip occurred on a newly propagated fault called North Chelungpu Chinshui detachment, which coincides with the area where the abnormally smooth rupture dynamics was observed.

*A1.6: The Iwate sequence (Japan)*

The Iwate event occurred on June 13, 2008, at 23:43:53.2 in northern Japan. The CMT catalog indicates the epicentral location: 39.03N, 14.85E. The centroid depth of the earthquake was at 12 km. Its half-duration was 6.7 sec, for a moment magnitude $M_{wCMT} = 6.9$, and a coda magnitude (this work) $M_{wCODA} = 6.90$. The magnitude of the Japanese Meteorological Agency was $M_j = 7.2$. The focal mechanism of the main shock was that of a pure thrust with a dip angle of $42^0$. The coseismic displacement was inferred from InSAR data by Takada et al. (2009), who proposed a complex rupture that took place over five different planes and Ohta et al. (2008) provided a coseismic fault slip model on three subfaults, based on data from a dense GPS network, with a maximum slip of 3.5 m on the southern fault segment.

The seismic sequence used in this study contains 5 aftershocks ($4.60 \le M_w \le 5.62$). Wang et al. (2008) described a distinctive, anomalous low-$V_P$, low-$V_S$, and low-Poisson ratio in the upper 10 km of the crust, where the fault strength may be weaker than in other regions of the seismogenic layer, which was interpreted as due to the presence of fluids from slab dehydration. The hypocentral depth from regional data was 8 km (Wang et al., 2008), well above the subducting Pacific plate (the slab depth in the Iwate epicentral area is between 100 and 150 km), and just to the East of the volcanic belt of NE Japan.

The Iwate earthquake is not a subduction earthquake, but results from the compressional rupture of a shallow crustal structure, which is probably in a tectonic environment characterized by high pore-fluid pressure.

This sequence (see bottom frame in Figure A11) shows a familiar behavior: the small events are almost self-similar, but a jump in Brune stress drop is needed to match the corner frequency of the main shock. According to the $M_0$ $vs.$ $f_c$ plot, the computed dynamic friction coefficients (Figure A11, top frame) are about constant for all the aftershocks, with a slight decrease (lubrication) for the main shock.

The Iwate fault is clearly not a mature one, and the fits of Figure A12 confirm the break in self-similarity with respect to the main shock that may be inferred after the visual inspection of Figure A11. Finally, the complex fault architecture responsible for the Iwate mainshock is compatible with the presence of a wide damage zone that dominates its permeability structure. In terms of the Caine's (1996) classification, we think that Iwate and Hector Mine may be very similar. The limited amount of apparent dynamic lubrication seen in Figure A11, compared with the results obtained for the Hector Mine fault zone (Figure A7) indicate a similar behavior for the two structures, with the Iwate fault plane (the only thrust fault analyzed) characterized by the largest shear pre-stress of all the faults sampled in this study.

## A2: Scaling of dynamic stress drop with radiated energy

For a mixed mode II-III fracture with constant rupture velocity and homogeneous dynamic stress drop, we derive the following expression for the crack's dynamic stress drop:

$$\Delta\sigma = F(\gamma,\varepsilon,\zeta,k)\sigma_a,$$

where $\sigma_a = \mu \frac{E_R}{M_0}$ is the apparent stress, and $F(\gamma,\varepsilon,\zeta,k)$ is a function of four dimensionless parameters.

Our energy-based estimates of dynamic stress drop correlate very strongly with the corresponding values of the Brune's stress parameter, but with substantially smaller uncertainties.

Crack models have long been used in seismology for the quantitative description of the ground motion observed spectra; the most widely used one was developed by Brune (1970, 1971): an earthquake dislocation is described as a tangential stress pulse instantaneously applied to the interior of a dislocation surface, and the resulting time function of the dislocation motion is directly related to the effective stress available to accelerate the two sides of the faults. The Brune crack model does satisfactorily describe the near-field and the far-field displacement time-functions and Fourier amplitude spectra of point-source earthquakes. Such capabilities, together with the simplicity of use, are the most important contributions to its widespread success.

Even today, the Brune stress drop is a common estimate of the dynamic stress drop, which is determined from the zero-frequency level ($\Omega_0$), and the corner frequency ($f_c$) of the far-field displacement amplitude spectrum. Snoke (1987) found "*remarkable that the application of such a simple model has resulted in easily interpretable scaling relations among source parameters for many suites of earthquakes*".

However, the physical description of faulting given in the Brune model suffers for an important oversimplification of the entire phenomenon. Moreover, as we will show later, the uncertainties associated to the Brune stress drops from corner frequency measurements may be too large for these parameters to be effectively used for the investigation of the thermal characteristics of faulting, because of the amplification of the errors on the corner frequencies through their formal propagation.

More recently, dynamic fracture models were based on the calculation of energy balance at the crack tip, where the most important physical processes take place during fracture propagation. Important reviews of the basic principles of dynamic fracture mechanics are, among others, those by Kostrov and Das (1988), Freund (1990), and Broberg (1999).

If friction on the actively slipping fault surface remains low after break-down, it may be considered as time-independent except in a small region near the crack edge (i.e. the breakdown region where the friction drops abruptly during rupture advancement). In this case, it can be shown that the amount of radiated energy $E_R$ can be stated in terms of a difference of energy flow at the propagating tip of the crack only (Freund, 1990, p. 293, eq. 5.8.18):

$$E_R = \int_{-\infty}^{+\infty} \left( \overline{F}_0(t') - \overline{F}(t') \right) dt' \qquad (1)$$

Here $\overline{F}_0(t)$ and $\overline{F}(t)$ stand for the instantaneous rate of energy flow into crack tip, integrated along the crack edge, in the case of quasi-static and dynamic crack propagation, respectively. $\overline{F}$ and $\overline{F}_0$ are in units of force×length/time ($J \cdot \sec^{-1}$ or $N \cdot m \cdot \sec^{-1}$). Since a static crack does not radiate, the difference between the static and the dynamic case equates to the radiated amount in the crack energy balance. Adapting the definitions from (Freund, 1990), we may write:

$$\overline{F}(t) = \int_{\Lambda(t)} F(s, t)\, ds \qquad (2)$$

where s is the position along the crack edge and $\Lambda$(t) the crack perimeter at time t, and $F(s, t)$ is the instantaneous flow at a given position s along the crack edge and at time tIn order to estimate $\overline{F}$ and $\overline{F}_0$, by assuming a simple crack model, we may relate them to the stress intensity factors $K_{II}$ and $K_{III}$ through the definition of the energy flow $G$, or the rate of mechanical energy flow out of the body and into the crack tip per unit crack advance, and per unit length of crack edge, according to (Freund, 1990, eq. 5.3.2):

$$G(t) = \lim_{\Gamma \to 0} \left\{ \frac{F(\Gamma)}{V_r} \right\} \qquad (3)$$

and, under the usual assumption that the breakdown region and $\Gamma$ are reasonably small, we can get rid of the limit, and, upon integrating on position $s$ around the crack edge $\Gamma$, we obtain:

$$\overline{F}(t) = \int_{\Lambda} V_r(s) G(t, s)\, ds \qquad (4)$$

$$\overline{F}_0(t) = \int_{\Lambda} V_r(s) G_0(t, s)\, ds. \qquad (5)$$

For simplicity, we henceforth reduce our analysis to the simple case of radial symmetry (circular crack expanding at constant velocity $V_r$) and constant material properties. For a circular crack of diameter $L(t)$, equations (4) and (5) become:

$$\overline{F}(t) = V_r\, L(t) \int_0^{2\pi} G(t, \theta)\, d\theta \qquad (6)$$

$$\overline{F_0}(t) = V_r \; L(t) \int_0^{2\pi} G_0(t,\theta)\, d\theta \qquad (7)$$

For mixed mode cracks, (Broberg, 1999), if we neglect opening (mode I) for tectonic earthquake faults, we can relate $G$ to the stress intensity factors and to the Yoffe functions as:

$$G = G_{II} + G_{III} = \frac{1}{4(1-k^2)\mu} K_{II}^2 \; Y_{II}(k,\zeta) + \frac{1}{2\mu} K_{III}^2 \; Y_{III}(\gamma) \qquad (8)$$

where Yoffe function $Y_{II}(k,\zeta)$ and $Y_{III}(\gamma)$ are functions of the velocity ratios $\zeta = V_r / c_P$, $k = \sqrt{(1-2\nu)/(2-2\nu)} = c_S / c_P$ and $\gamma = V_r / c_S$ (from Broberg, 1999, equations: (3.5.15), (3.5.16), and (3.5.17)).

For the stress intensity factors, assuming a mixed mode where $\theta$ is the angle between slip direction and the local propagation direction of the crack edge, we may define:

$$K_{II} = \cos(\theta) \Delta\sigma_D \sqrt{\frac{\pi L}{2}}\, \chi_{II}(k,\zeta) \qquad (9)$$

(modified from Broberg, 1999, eq. 6.9.90), and:

$$K_{III} = \sin(\theta) \Delta\sigma_D \sqrt{\frac{\pi L}{2}}\, \chi_{III}(\gamma), \qquad (10)$$

where, again, $\chi_{II}(k,\zeta)$ and $\chi_{III}(\gamma)$ are functions of the velocity ratios defined above (modified from Broberg, 1999, eq. 6.9.147), and $\Delta\sigma_D$ indicates the dynamic stress drop. We introduced the amplitude factors $\cos(\theta)$ and $\sin(\theta)$ to account for the mixed mode fracture. On the edge of the crack propagating perpendicular to the slip direction, $\theta = 90$ and only $K_{III}$ is nonzero. On the edge propagating parallel to slip, only $K_{II}$ remains, whereas on an intermediate location a mix of both modes will be active. Note that in the quasi-static case $\gamma = \zeta = 0$, so the right-hand side fractions in $K_{II}$ and $K_{III}$ equate to 1. Finally, we may write:

$$G(t) = \frac{\pi \Delta\sigma_D^2 L(t)}{4\mu} \left\{ \frac{\cos^2\theta}{(1-k^2)} \Phi_{II} + \sin^2\theta \; \Phi_{III} \right\} \qquad (11)$$

$$G_0(t) = \frac{\pi \Delta\sigma_D^2 L(t)}{4\mu} \left\{ \frac{\cos^2\theta}{(1-k^2)} + \sin^2\theta \right\} \qquad (12)$$

where $\Phi_{II} = Y_{II}\, \chi_{II}$ and $\Phi_{III} = Y_{III}\, \chi_{III}$ are functions of the velocity ratios only.

*Radiated energy and dynamic stress drop*

By combining equations (1), (2), (3), (16), (7):

$$E_R = \int_{t'} \left(\overline{F}_0(t') - \overline{F}(t')\right) dt' \tag{13}$$

$$E_R = \int_t V_r \frac{L(t)}{2} \left\{ \int_0^{2\pi} G(t,\theta) - G_0(t,\theta)\, d\theta \right\} dt \tag{14}$$

$$\int_0^{2\pi} \left(G(t,\theta) - G_0(t,\theta)\right) d\theta \tag{15}$$

$$= \frac{\pi \Delta\sigma_D^2 L(t)}{4\mu} \int_0^{2\pi} \left( \cos^2\theta \, \frac{1-\Phi_{II}}{(1-k^2)} + \sin^2\theta \left(1-\Phi_{III}\right) \right) d\theta \tag{16}$$

$$= \frac{\pi^2 \Delta\sigma_D^2 L(t)}{4\mu} \left( \frac{1-\Phi_{II}}{(1-k^2)} + 1 - \Phi_{III} \right) \tag{17}$$

and write the coefficient $\mathrm{Z}$ for the rupture velocity function

$$\mathrm{Z} = \left( \frac{1-\Phi_{II}}{(1-k^2)} + 1 - \Phi_{III} \right) \tag{18}$$

While $\mathrm{Z}$ may be computed for the case of a circular, sharp/edged crack propagating at a constant velocity with the above equation, it has no relevance for real earthquakes where rupture is a more complex process. In that case we consider $\mathrm{Z}$ as a dimensionless coefficient that may be estimated empirically from the data.

$$E_R = \frac{V_r \pi^2 \Delta\sigma_D^2}{8\mu} \mathrm{Z} \int_t L^2(t)\, dt \tag{19}$$

$$= \frac{V_r \pi^2 \Delta\sigma_D^2}{8\mu} \mathrm{Z} \int_0^T (2tV_r)^2\, dt \tag{20}$$

At this point we may use the rupture duration

$$\mathrm{T} = \frac{L(\infty)}{2V_r} \tag{21}$$

in order to write:

$$\int_0^T (2V_r t')^2\, dt' = \frac{4}{3} T^3 V_r^2 \tag{22}$$

we finally obtain:

$$E_R = \frac{\pi^2 \Delta\sigma_D^2}{8\mu} Z \frac{4}{3} T^3 V_r^3 \qquad (23)$$

by using the definition (21) of rupture duration:

$$E_R = \frac{\pi^2 \Delta\sigma_D^2}{48\mu} Z L^3(\infty) \qquad (24)$$

When rupture velocity tends to zero, $T^3 V_r^3$ remains constant for a given rupture dimension, however $\Phi_{II}$ and $\Phi_{III}$ tend to one so that the radiated energy tends to zero. About the assumption of constant propagation velocity, this implicitly neglects the radiated energy in the starting (accelerating) and stopping (decelerating) phases of fracture. However, the faulting size in the starting phase is small, while the duration of the stopping phases can be expected to be short and at a reduced value of rupture velocity $V_r$, so that the contribution to $E_R$ from those phases may be less relevant.

The next step is the quantification of the stress drop as a function of the seismic moment, and of the crack radius. From the definition of seismic moment:

$$M_0 = \mu A < d > \qquad (25)$$

From Eshelby (1957, 1959):

$$< d > = \frac{16}{7\pi} \frac{\Delta\sigma}{\mu} \left( \frac{L(\infty)}{2} \right) \qquad (26)$$

so that:

$$\Delta\sigma = \mu < d > \frac{7\pi}{8L(\infty)} \qquad (27)$$

Substituting (27) into (25):

$$M_0 = \frac{2}{7} \Delta\sigma L^3(\infty) \qquad (28)$$

and:

$$L(\infty) = \left( \frac{7M_0}{2\Delta\sigma} \right)^{1/3} \qquad (29)$$

Using again the definition (21) of rupture duration in (29), and substituting in (24):

$$E_R = \frac{\pi^2 \Delta\sigma_D^2}{48\mu} Z \left( \frac{7M_0}{2\Delta\sigma_S} \right) \qquad (30)$$

Using $\Delta\sigma_S = \varepsilon \Delta\sigma_D$:

$$E_R = f(\gamma,\zeta,\varepsilon,k)\frac{7\pi^2\Delta\sigma_D M_0}{96\mu} \quad (31)$$

with

$$f(\gamma,\zeta,\varepsilon,k)=\frac{\mathrm{Z}}{\varepsilon} \quad (32)$$

From (30), (31), (32) we can write:

$$\Delta\sigma_D = \frac{96}{7\,\pi^2 f(\gamma,\zeta,\varepsilon,k)}\mu\frac{E_R}{M_0} \quad (33)$$

$$= F(\gamma,\zeta\ \varepsilon,k)\,\sigma_a \quad (34)$$

where:

$$\sigma_a = \mu\frac{E_R}{M_0} \quad (35)$$

is called the apparent stress (Wyss, 1970).

We may now write our relationship for radiated energy and stress drop as:

$$\Delta\tau_d = F\ \mu\frac{E_R}{M_0}, \quad (36)$$

where, in the theoretical case of an expanding circular crack with a sharp tip, $F$ is defined above. However, in natural earthquakes fracture propagation is a more complex, heterogeneous process and differs in several ways from the simplified circular sharp crack model. In particular, the entire fault area is not slipping owing to the presence of barriers (stronger patches) and the fracture tip is not sharp but rather expanded over a process region of finite length. It is expected that the value of $F$ obtained for the sharp crack model may represent a lower bound for natural earthquakes, which, due to their reduced crack tip singularity and their reduced slipping area, are likely to radiate less energy for a similar amount of stress drop.

As a consequence, we rather estimate a value of $F$ by assuming that, within the whole investigated dataset, the lowest value of the sliding friction coefficient corresponds to a situation where the residual dynamic friction is negligible (this case corresponds to the largest of the twin main shocks of the San Giuliano sequence, see appendix A1.1). In other words, we assume that the dynamic stress drop for such event is total. While this assumption represents an ideal lower bound, it is in part justified by several experimental results (Di Toro et al., 2006, 2004) showing that, under favorable circumstances and seismic slip conditions, the dynamic friction coefficient may drop down to values as low as 0.05. Thus we obtain an estimate $F \approx 3$, which, owing to the assumption of total stress drop, is obviously an upper bound for the value of $F$. Taking smaller values reduces the difference between events in term of stress drops, but the fundamental observation of gradual weakening remains unaltered. We do not show the effect of increasing $F$, as it is in all ways similar to that induced by an increase in the pore pressure as illustrated in Fig. A2, A4, A6, A8, A10, and A12 within this Appendix, as well as in Fig. 3 of the main report.

## Acknowledgements

Many thanks to Giulio Di Toro for his thoughtful review. Kevin Mayeda was supported under Weston Geophysical subcontract No. GC19762NGD and AFRL contract No. FA8718-06-C-0024. Work by L. Malagnini was performed under the auspices of the Dipartimento della Protezione Civile, under contract S3 – INGV-DPC (2007-2009), project: "Valutazione rapida dei parametri e degli effetti dei forti terremoti in Italia e nel Mediterraneo".

## References

Amato, A., et al. (1998), The 1997 Umbria-Marche, Italy, Earthquake Sequence: A First Look at the Main Shocks and Aftershocks, *Geophys. Res. Lett.*, *25*(15), 2861–2864.

Barton, C.A., M.D. Zoback, and D. Moos (1995). Fluid flow along potentially active faults in crystalline rock, *Geology*, 23, n. 8, pp. 683-686.

Boncio, P. (2008) - Deep-crust strike-slip earthquake faulting in southern Italy aided by high fluid pressure: insights from rheological analysis. In: WIBBERLEY et al. (Eds.) The internal structure of fault zones: implications for mechanical and fluid-flow properties. *Special publication of the Geological Society of London*, 299, Ch. 11, DOI: 10.1144/SP299.11.

Broberg, B.K. (1999). Cracks and fracture, Academic Press, ISBN 0121341305, 9780121341305, 752 pp.

Brodsky, E. E. and H. Kanamori (2001). The elastohydrodynamic lubrication of faults, *J. Geophys. Res.,* 106, 16, 357-16, 374.

Brune, J. N., T. L. Henyey, and R. F. Roy (1969), Heat flow, stress, and rate of slip along the San Andreas fault, California*, J. Geophys. Res*., 74, 3821 – 3827.

Brune, J. N. (1970). Tectonic stress and the spectra of seismic shear waves from earthquakes, *J. Geophys. Res.* 75, 4997-5009.

Brune, J. N. (1971 ). Correction (to Brune (1970)), *J. Geophys. Res.* 76, 5002.

Chiodini, G., C. Cardellini, A. Amato, E. Boschi, S. Caliro, F. Frondini, and G. Ventura (2004). Carbon dioxide Earth degassing and seismogenesis in central and southern Italy. *Geophys. Res. Lett*., 31, doi:10.1029/2004GL019480.

Caine, J.S., J.P. Evans, and C.B. Forster (1996). Fault zone architecture and permeability structure, *Geology,* 24; 1025-1028, doi: 10.1130/0091-7613(1996).

Carslaw, H.S., and J.C. Jaeger (1959). Conduction of Heat in Solids, Oxford Univ Press.

De Paola, N., T. Hirose, T. Mitchell, G. Di Toro, T. Togo, and T. Shimamoto (2008). Thermal Pressurization Induced by Coseismic Shear Heating Within Thermally Unstable Rocks, *Eos Trans. AGU, 89*(53), Fall Meet. Suppl., Abstract S34B-07.

Di Toro, G., D.L. Goldsby, and T.E. Tullis, Friction falls towards zero in quartz rock as slip velocity approaches seismic rates, *Nature, 427*, 436-439, (2004).

Di Toro, G., Hirose, T. Nielsen, S., Pennacchioni, G. and T. Shimamoto (2006). Natural and experimental evidence of melt lubrication of faults during earthquakes, *Science*, 311, 647-649, doi:10.1126/science.1121012.

Doan, M. L., E. E. Brodsky, Y. Kano, and K. F. Ma (2006). In situ measurement of the hydraulic diffusivity of the active Chelungpu fault, Taiwan. *Geophys. Res. Lett*, 33, L16317, doi: 10.1029/2006GL026889.

Eshelby, J.D. (1957). The determination of the elastic field of an ellipsoidal inclusion, and related problems, *Proc. Roy. Soc. Lond*., A241, 376-396.

Eshelby, J. D. (1959), The elastic field outside an ellipsoidal inclusion, *Proc. R. Soc. London, Ser. A*, *252*, 561–569.

Freund, L.B. (1990). Dynamic fracture mechanics, Cambridge Monograph on Mechanics and Applied Mathematics, Cambridge University Press, Cambridge, 563 pp.

Grawinkel, A., and Stockhert, B. (1997). Hydrostatic pore fluid pressure to 9 km depth : Fluid inclusion evidence from the KTB deep drill hole, *Geophys. Res. Lett.,* vol. 24, n° 24, pp. 3273-3276.

Griffith, W.; G. Di Toro, G.; Pennacchioni, D. Pollard, and S. Nielsen (2009). Static stress drop associated with brittle slip events on exhumed faults *J. Geophys. Res.*, 114, B02402.

Famin, V., S. Nakashima, A.M. Boullier, K. Fujimoto and T. Hirono (2008). Earthquakes produce carbon dioxide in crustal faults, *Earth and Planetary Science Letters* 265 (3–4), pp. 487–497, doi:10.1016/j.epsl.2007.10.041.

Han, R., T. Hirose, and T. Shimamoto (2009). Strong velocity weakening and powder lubrication of simulated carbonate faults at seismic slip rates, *J. Geophys. Res.*, in press.

Han, R. T. Shimamoto, T. Hirose, J-H Ree, and J. Ando, (2007) Ultralow friction of carbonate faults caused by thermal decomposition, *Science*, *316*, 878-881, (2007).

Heaton, T.H. (1990). Evidence for and implications of self-healing pulses of slip in earthquake rupture, *Phys. Earth Planet Int.,* 64, 1-20.

Hirose, T., and M. Bystricky (2007). Extreme weakening of faults during dehydration by coseismic shear heating, *Geophys. Res. Lett.,* 34, L14311, doi:10.1029/2007GL030049.

Hunt, J.M. (1990). Generation and migration of petroleum from abnormally pressured fluid compartments, *Am. Ass. Petroleum Geol. Bull.,* 74, pp. 1-12.

Ide, S. and G. C. Beroza (2001). Does apparent stress vary with earthquake size?, *Geophys. Res. Lett.* 28, 3349-3352.

Ishikawa, T., M. Tanimizu, K. Nagaishi, J. Matsuoka, O. Tadai, M. Sakaguchi, T. Hirono, T. Mishima, W. Tanikawa, W. Lin, H. Kikuta, W. Soh, and S.-R. Song (2008), Coseismic fluid–rock interactions at high temperatures in the Chelungpu fault, *Nature Geoscience*, 1, 679-683, doi:10.1038/ngeo308.

Izutani, Y. (2005). Radiated energy from the mid Niigata, Japan, earthquake of October 23, 2004, and its aftershocks, *Geophys. Res. Lett.*, 32, L21313, doi:10.1029/2005GL024116.

Ito, T., and M.D. Zoback (2000). Fracture permeability and in situ stress to 7 km depth in the KTB Scientific Drillhole, *Geophys. Res. Lett.,* 27, n. 7, pp. 1045-1048.

Kanamori, H., and T. Heaton (2000). Microscopic and macroscopic physics of earthquakes, contained in Geocomplexity and the Physics of Earthquakes, Editors J.

Rundle, D. Turcotte, and W. Klein, Geophysical Monograph 20, Published by the American Geophysical Union, D.C., 127-141.

Kano, Y., J. Mori, R. Fujio, H. Ito, T. Yanagidani, S. Nakao, and K.-F. Ma (2006). Heat signature on the Chelungpu fault associated with the 1999 Chi-Chi, Taiwan earthquake, *Geophys. Res. Lett* ., 33, L14306, doi:10.1029/2006GL026733.

Kostrov, B.V., and S. Das (1988). Principles of Earthquake source dynamics, Cambridge Monograph on Mechanics and Applied Mathematics, Cambridge University Press, Cambridge, 286 pp.

Latorre D., De Gori P., Chiarabba C., Amato A., Virieux J. and Monfret T. (2008), Three-dimensional kinematic depth migration of converted waves: application to the 2002 Molise aftershock sequence (southern Italy), *Geophysical Prospecting*, 56, 587-600, DOI: 10.1111/j.1365-2478.2008.00711.x

Ma, K. F., Tanaka, H., Song, S. R., Wang, C. Y., Hung, J. H., Tsai, Y. B., Mori, J., Song, Y. F., Yeh, E. C., Soh, W., Sone, H., Kuo, L. W., and Wu, H. Y. (2006). Slip zone and energetics of a large earthquake from the Taiwan Chelungpu-fault Drilling Project, Nature, 444, 473–476, doi:10.1038/nature05253.

Ma, K.-F., E.E. Brodsky, J. Mori, C. Ji, T.R. A. Song, and H. Kanamori (2003). Evidence for fault lubrication during the 1999 Chi-Chi, Taiwan earthquake (Mw7.6) *Geophys. Res. Lett.,* **30** (5), 1244, doi:10.1029/2002GL015380.

Malagnini, L., and K. Mayeda (2008). High-stress strike-slip faults in the Apennines: An example from the 2002 San Giuliano earthquakes (southern Italy), *Geophys. Res. Lett.*, *35*, L12302, doi:10.1029/2008GL034024.

Malagnini, L., L. Scognamiglio, A. Mercuri, A. Akinci, and K. Mayeda (2008), Strong evidence for non-similar earthquake source scaling in central Italy, *Geophys. Res. Lett*., 35, L17303, doi:10.1029/2008GL034310.

Mayeda, K., and L. Malagnini (2009). An evolution of a new spectral ratio technique for the analysis of source scaling: an application to the Chi-Chi sequence, *Geophys. Res. Lett*., 36, L10308, doi: 10.1029/2009GLD37421.

Mayeda, K., L. Malagnini, and W.R. Walter (2007), A new spectral ratio method using narrow band coda envelopes: Evidence for non-self-similarity in the Hector Mine sequence, *Geophys. Res. Lett.*, *34*, L11303, doi:10.1029/2007GL030041.

Mayeda, K., and W.R. Walter (1996). Moment, energy, stress drop and source spectra of Western U.S. earthquakes from regional coda envelopes, *J. Geophys. Res.*, 101, 11,195-11,208.

Madariaga, R., (2007), Slippery when hot, *Science*, Vol. 316. no. 5826, pp. 842 – 843, DOI: 10.1126/science.1142332.

Melosh, H.J (1996). Dynamical weakening of faults by acoustic fluidization, *Nature* 379, 601-606, doi:10.1038/379601a0.

Miller, S.A., C. Collettini, L. Chiaraluce, M. Cocco, M. Barchi, and B.J.P. Kaus (2004). Aftershocks driven by a high-pressure $CO_2$ source at depth, *Nature*, 427, 724-727.

Montone, P., A. Amato, and S. Pondrell (1999). Active stress map of Italy, J. Geophys. Res., 104, B11, pp. 25595-25610.

Nadeau, R. M., and L.R. Johnson (1998). Seismological studies at Parkfield VI: Moment release rates and estimates of source parameters for small repeating earthquakes Bull. Seismol. Soc. Am., 88, 790–814.

Nielsen, S., G. Di Toro, T. Hirose, and T. Shimamoto (2008), Frictional melt and seismic slip, *J. Geophys. Res.*, *113*, B01308, doi:10.1029/2007JB005122.

Noda, H., and N. Lapusta (2009). 3D earthquake sequence simulations with frictional heating and hydro-thermo-mechanical effects (abstract), *seminar given on October 12, 2009 at Istituto Nazionale di Geofisica e Vulcanologia, Rome, Italy*.

Ohta, Y., M. Ohzono, S. Miura, and T. Iin (2008). Coseismic fault model of the 2008 Iwate-Miyagi Nairiku earthquake deduced by a dense GPS network *Earth Planets Space*, 60, 1197-1201, 2008.

Peltzer, G. P. Rosen, F. Rogez, and K. Hudnut (1996). Postseismic rebound in fault step-overs caused by pore fluid flow, *Science*, 273, 1202-1204.

Rempel, A. W., and J. R. Rice, Thermal pressurization and onset of melting in fault zones, *J. Geophys. Res.*, 111, B09314, doi:10.1029/2006JB004314, (2006).

Revenaugh, J., and C. Reasoner (1997). Cumulative offset of the San Andreas fault in central California: A seismic approach, *Geology*, 25; no. 2; p. 123-126; doi: 10.1130/0091-7613(1997)025<0123:COOTSA>2.3.CO;2.

Rice, J. R., Heating and weakening of faults during earthquake slip, *J. Geophys. Res.*, 111, doi:10.1029/2005JB004006, (2006).

Shipton, Z.K., A.M. Soden, J.D. Kirkpatrick, A.M Bright, and R.J. Lunn (2006). How thick is a fault? Fault displacement-thickness scaling revisited, in: *Earthquakes: radiated energy and the physics of faulting, Geophysical Monograph Series 170*, doi: 10.1029/170GM19.

Sibson, R.H. (1974). Frictional constraints on thrust, wrench and normal faults, *Nature* 249, 542 – 54, doi:10.1038/249542a0.

Sibson, R.H. (1990). Rupture nucleation on unfavorably oriented faults, *Bull Seism. Soc. Am.,* 80, n. 6, pp 1580-1604.

Sibson, R.H. (1992a). Implications of fault-valve behaviour for rupture nucleation and recurrence, *Tectonophysics*, 211, pp. 283-293.

Sibson, R.H. (1992b). Fault-valve behavior and the hydrostatic-lithostatic fluid pressure interface, Earth-Science Reviews, 32, pp. 141-144.

Sibson, R.H. (1994). Crustal stress, faulting and fluid flow, Geofluids: Origin, Migration and Evolution of Fluids in Sedimentary Basins, Parnell, J. (Ed.), Geol. Soc. Special Publication No. 78, pp. 69-84.

Sibson, R. H. (2007), An episode of fault-valve behavior during compressional inversion? The 2004 MJ 6.8 Mid-Niigata Prefecture, Japan earthquake sequence, *Earth Planet. Sci. Lett.*, 257, 188–199.

Snoke, J.A. (1987). Stable determination of (Brune) stress drops, *Bull. Seism. Soc. Am.,* 77, 530-538.

Spudich, P. (1998). Use of fault striations and dislocation models to infer tectonic shear stress during the 1995 Hyogo-ken Nanbu (Kobe), Japan, earthquake *Bull. Seismol. Soc. Am.,* 88, 413-427.

Suppe, J. (2007). Absolute fault and crustal strength from wedge tapers, *Geology*, 35, no. 12, p. 1127-1130, doi: 10.1130/G24053A.1.

Suppe, J., and L. F. Yue (2008). Pore-fluid pressures and crustal strength, Geophysical Research Abstracts, Vol. 10, EGU2008-A-01970, 2008 SRef-ID: 1607 - 7962/gra/EGU2008-A-01970, EGU General Assembly 2008.

Takada, Y., and T. Kobay (2009). Coseismic displacement due to the 2008 Iwate-Miyagi Nairiku earthquake detected by ALOS/PALSAR: preliminary results, *Earth Planets Space*, 61, e9-e12, 2009.

Tanikawa, W. and T. Shimamoto (2009). Frictional and transport properties of the Chelungpu fault from shallow borehole data and their correlation with seismic behavior during the 1999 Chi-Chi earthquake. *J. Geophys. Res.*, 114, B01402. doi:10.1029/2008JB005750.

Tanikawa, W., Shimamoto, T., Wey, W.K., Wu, W.Y., Lin, C.W., and Lai, W.C. (2004). Sedimentation and generation of abnormal fluid pressure in the focal area of 1999 Taiwan Chi-Chi earthquake, In: Proceedings of the ISRM In. Symp. 3rd ARMS, 553-557.

Townend, J., and M.D. Zoback (2000). How faulting keeps the crust strong, *Geology*, 28, n. 5, pp. 399-402.

Unsworth, M., G. Egbert, and J. Booker (1999). High-resolution electro-magnetic imaging of the San Andreas fault in Central California, J. Geophys. Res., 104 (B1) 1131-1150, doi: 10.1029/98JB01755.

Yue, L.F. (2007). Active structural growth in central Taiwan in relationship to large earthquakes and pore-fluid pressures [Ph.D. thesis]: Princeton, New Jersey, Princeton University, 173 p..

Yue, L.-F., J. Suppe, and J.-H. Hung (2005). Structural geology of a classic thrust belt earthquake: the 1999 Chi-Chi earthquake Taiwan ($M_w$=7.6). *J. Struct. Geol.,* 27, pp. 2058-2083.

Yue et al., (2005). Jour. Structural Geol.).

Wang, J.-H. (2009). Effect of Thermal Pressurization on Radiation Efficiency, Bull. Seism. Soc. Am. . 99, No. 4, pp. 2293–2304, doi: 10.1785/0120080187.

Wang, Z., Y. Fukao, S. Kodaira, and R. Huang (2008). Role of fluids in the initiation of the 2008 Iwate earthquake (M7.2) in northeast Japan, Geophys. Res. Lett., 35, L24303, doi: 10.1029/2008GL035869.

Wyss, M. (1970). Observation and interpretation of tectonic strain release mechanisms, *Ph.D. Thesis,* California Institute Technology, 1970.

Zoback, M.D., and J. Townend (2001). Implications of hydrostatic pore pressures at high crustal strength for the deformation of intraplate lithosphere, *Tectonophysics*, 336, pp. 19-30.

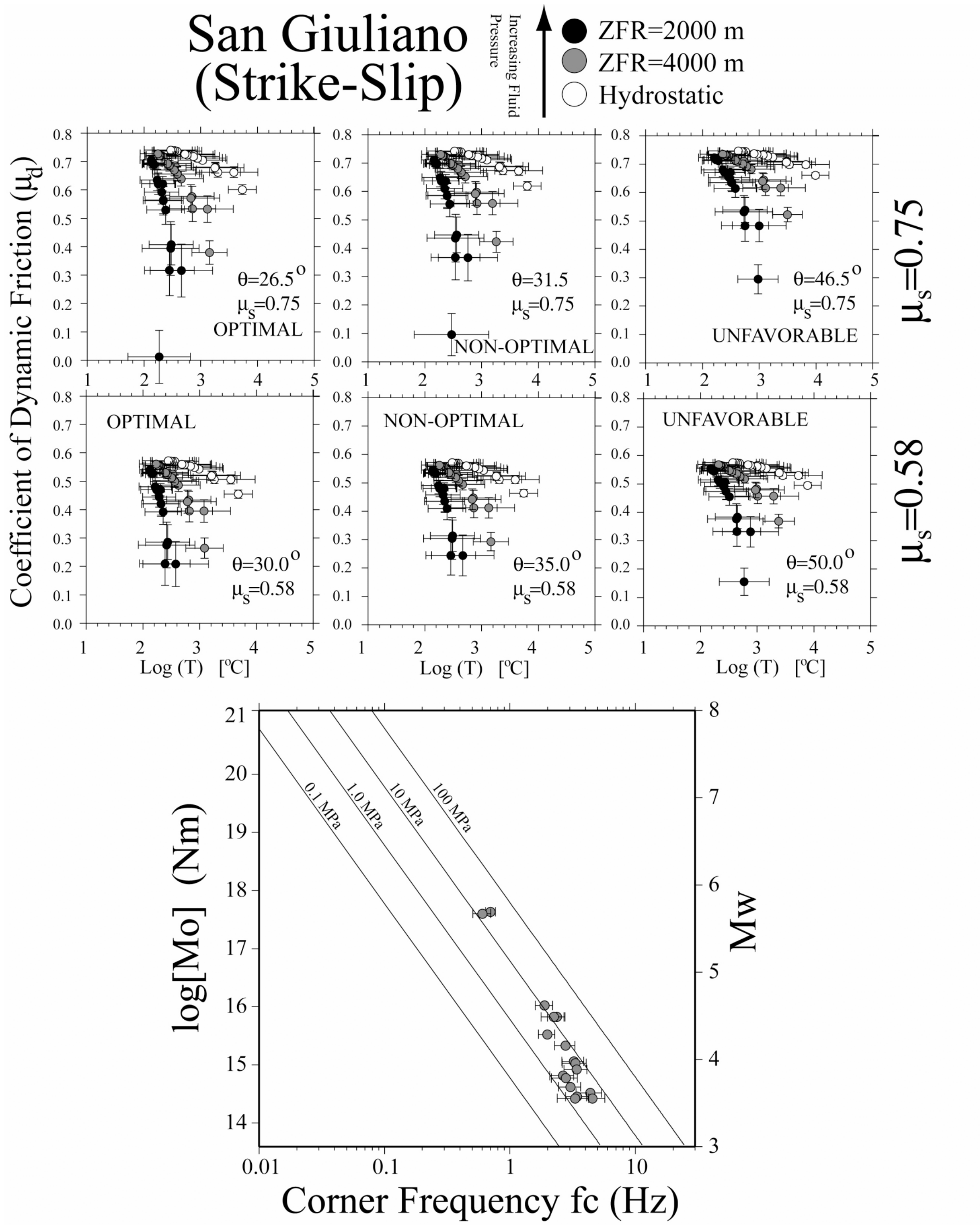


**Figure A1.** Top frames: coefficients of dynamic friction for the evens of the San Giuliano sequence, as a function of fault temperature. Darker symbols indicate shallower gradient transition depths, and thus higher pore fluid pressures. We sample two typical coefficients of static friction (0.75 and 0.58), and three orientations (optimal, optimal + 5 degrees, and optimal + 20 degrees. The latter orientation is called unfavorable, following Sibson, 1990). Of the six frames on dynamic friction, note that the largest event is missing in the two lower frames (left and middle). For those orientations, the coefficient relative to the larges event become negative (unacceptable). The coefficient F in equation (36) of Appendix A2 was calibrated to the value F=3.0 based on the hypothesis of total stress release for the largest mainshock of the sequence, in a situation of optimal orientation to the regional stress field.

Bottom frame: distribution of the seismic moments and corner frequencies for the San Giuliano sequence. The data set is consistent with a functional form: $M_0 \propto f_c^{-(3+\varepsilon)}$, with $\varepsilon = 0.9 \pm 0.3$.

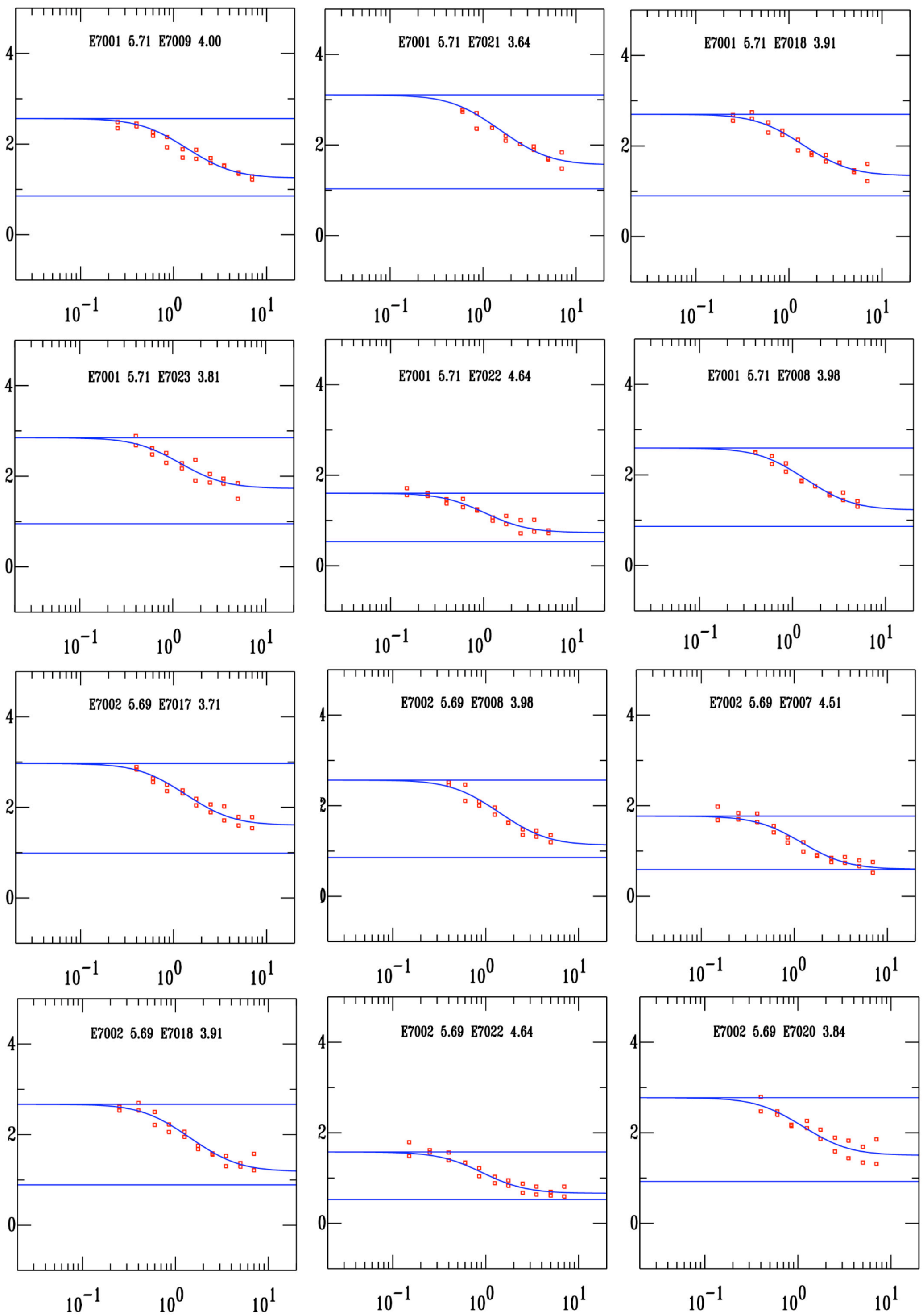


**Figure A2.** Fits between data (red squares) and the theoretical best scaling model (blue curve) for spectral ratios of the San Giuliano seismic sequence. Solid horizontal lines in blue represent the asymptotes expected for self-similar scaling. In the frame of each spectral ratio are indicated both the event identification numbers, with the earthquakes' moment magnitudes.

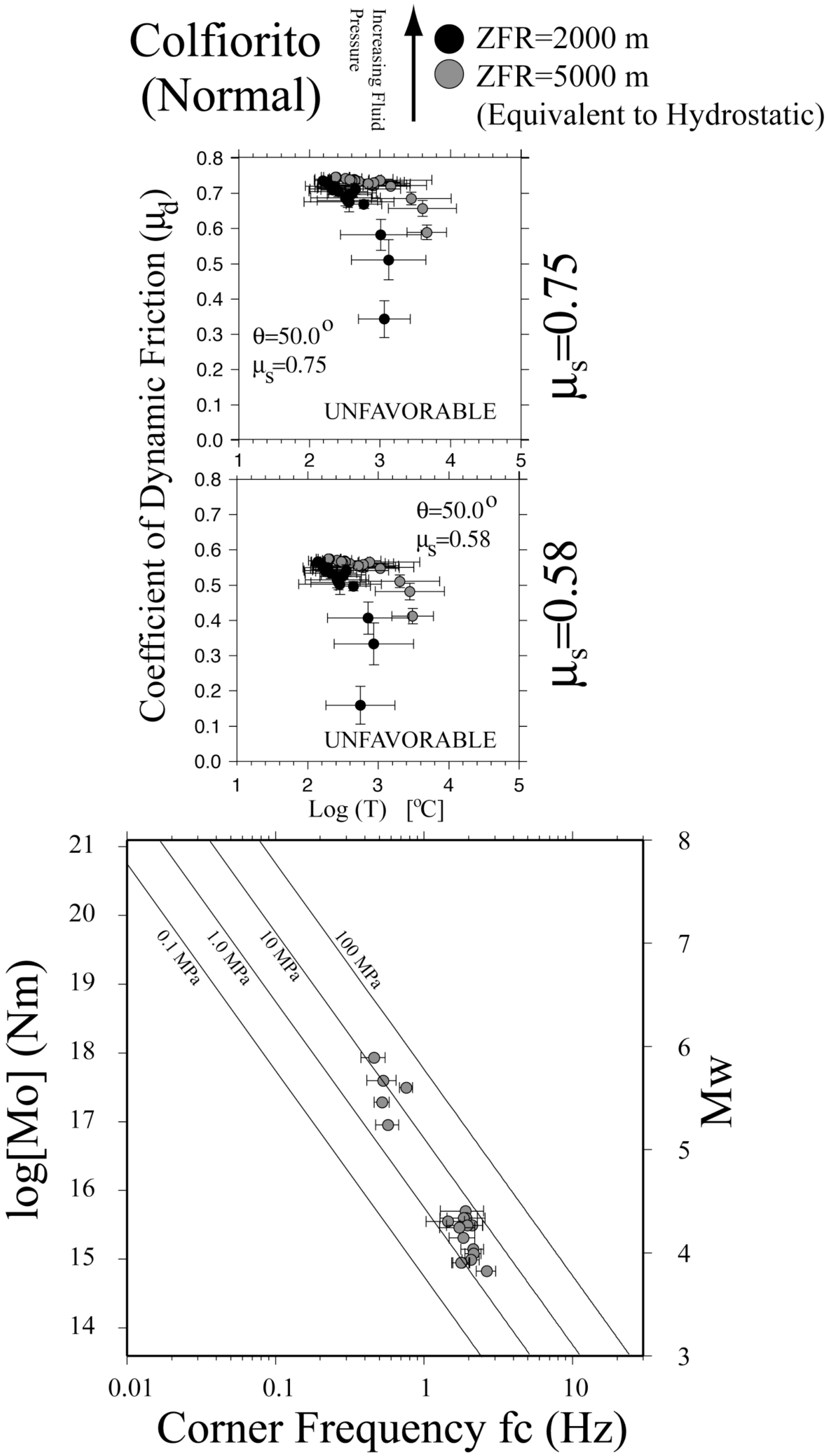
Colfiorito
(Normal)
Increasing Fluid Pressure
ZFR=2000 m
ZFR=5000 m
(Equivalent to Hydrostatic)
Coefficient of Dynamic Friction (μd)
θ=50.0°
μs=0.75
UNFAVORABLE
μs=0.75
θ=50.0°
μs=0.58
UNFAVORABLE
μs=0.58
Log (T) [°C]
log[Mo] (Nm)
Mw
0.1 MPa
1.0 MPa
10 MPa
100 MPa
Corner Frequency fc (Hz)

**Figure A3.** Top and middle frames: coefficients of dynamic friction for some evens of the Colfiorito sequence, as a function of the fault temperature. Darker symbols indicate shallower gradient transition depths, and thus higher pore fluid pressures. We sample two typical coefficients of static friction (0.75 and 0.58), and the orientation dictated by the dip of the fault plane that was observed in the sequence.

Bottom frame: distribution of the seismic moments and corner frequencies for the sequence. A functional form: $M_0 \propto f_c^{-(3+\varepsilon)}$, where: $\varepsilon = 1.5 \pm 0.6$, can be used to describe the plot.

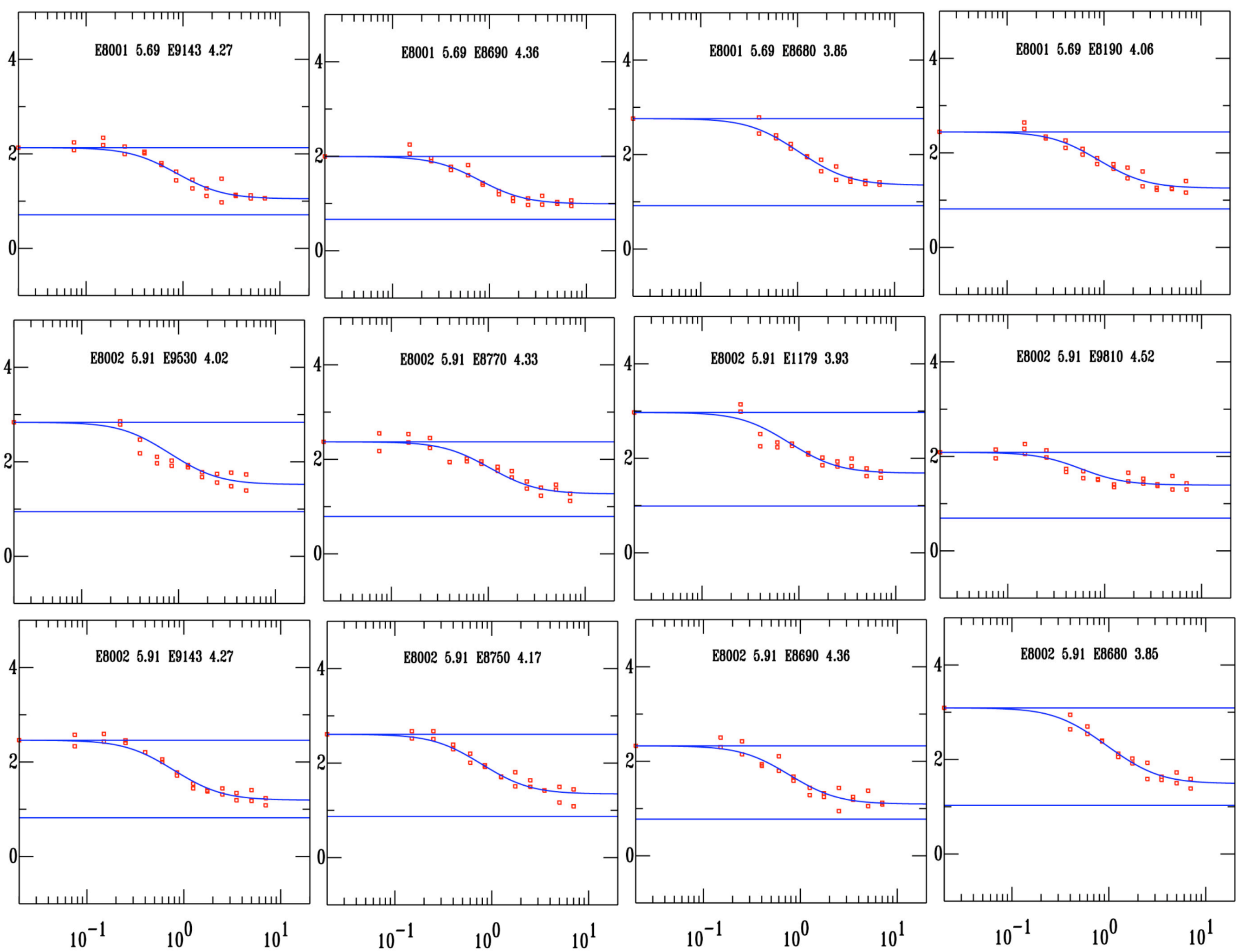


**Figure A4.** Fits between data (red squares) and the theoretical best scaling model (blue curve) for spectral ratios of the Colfiorito seismic sequence. Solid horizontal lines in blue represent the asymptotes expected for self-similar scaling. In the frame of each spectral ratio are indicated both the event identification numbers, with the earthquakes' moment magnitudes.

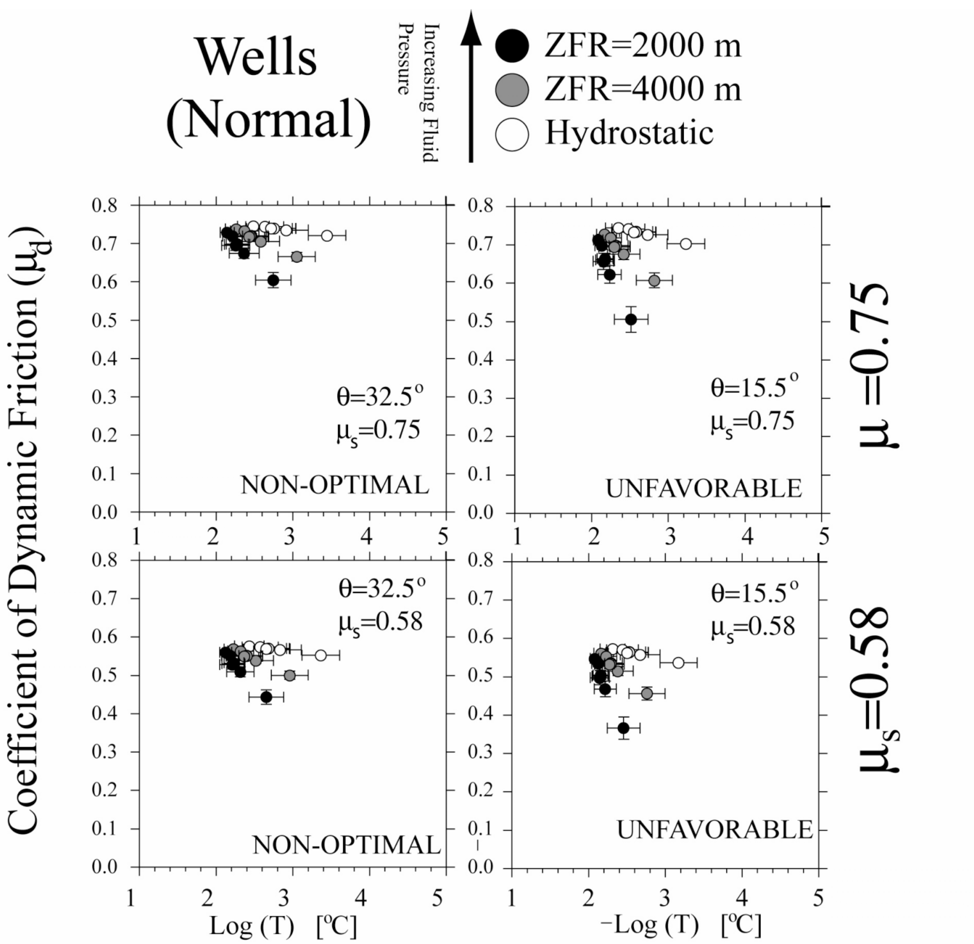
Wells
(Normal)
Increasing Fluid Pressure
ZFR=2000 m
ZFR=4000 m
Hydrostatic
Coefficient of Dynamic Friction ($\mu_d$)
θ=32.5°
$\mu_s$=0.75
NON-OPTIMAL
θ=15.5°
$\mu_s$=0.75
UNFAVORABLE
$\mu$=0.75
θ=32.5°
$\mu_s$=0.58
NON-OPTIMAL
θ=15.5°
$\mu_s$=0.58
UNFAVORABLE
$\mu_s$=0.58
Log (T) [°C]
−Log (T) [°C]

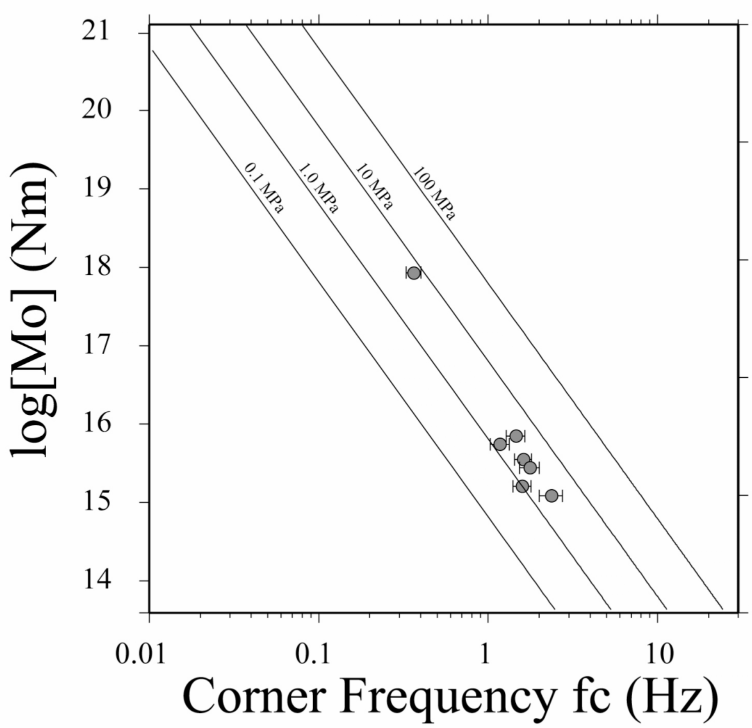
0.1 MPa
1.0 MPa
10 MPa
100 MPa
log[Mo] (Nm)
Mw
Corner Frequency fc (Hz)

**Figure A5.** Coefficients of dynamic friction as a function of the fault temperature for the evens of the Wells sequence. Darker symbols indicate shallower gradient transition depths, and thus higher pore fluid pressures. We sample two typical coefficients of static friction (0.75 and 0.58), and the orientations of the two conjugate planes dictated by the available moment-tensor solution.

Bottom frame: distribution of the seismic moments and corner frequencies for the sequence. The data set is consistent with a functional form: $M_0 \propto f_c^{-(3+\varepsilon)}$, with $\varepsilon = 1.0 \pm 0.2$.

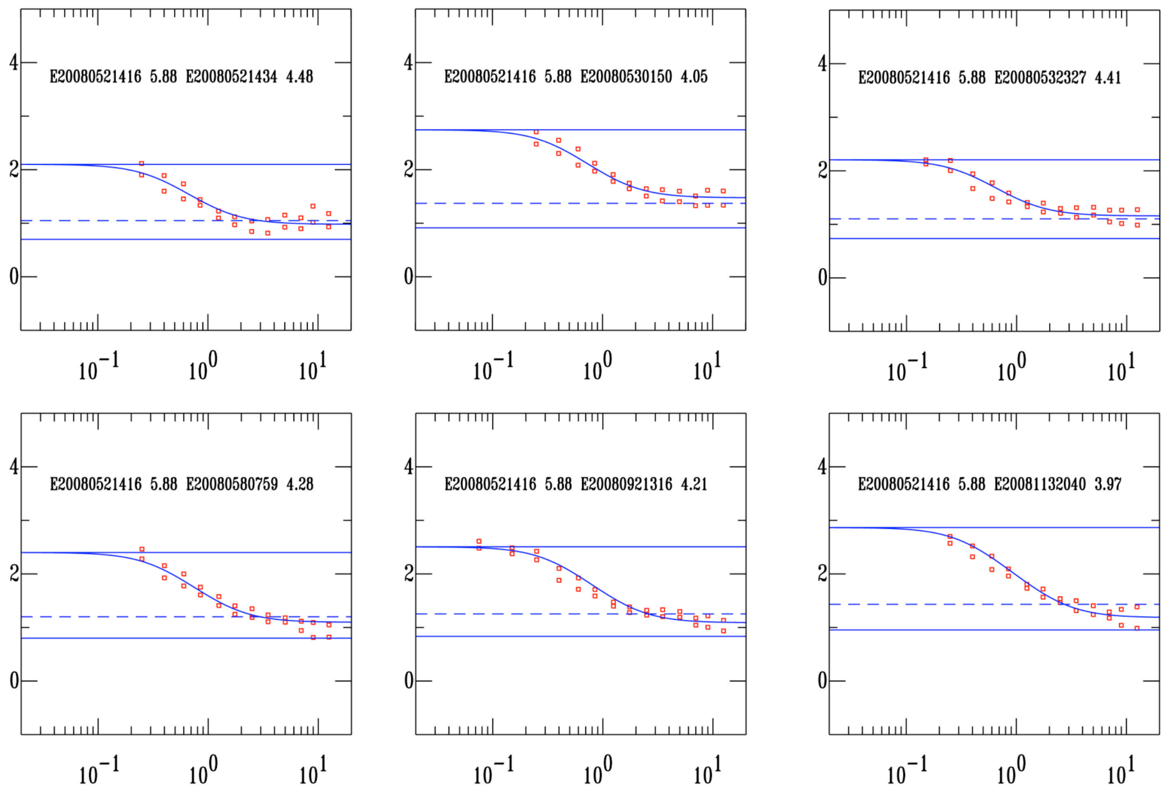


**Figure A6.** Fits between data (red squares) and the theoretical best scaling model (blue curve) for spectral ratios of the Wells seismic sequence. Solid horizontal lines in blue represent the asymptotes expected for self-similar scaling. In the frame of each spectral ratio are indicated both the event identification numbers, with the earthquakes' moment magnitudes.

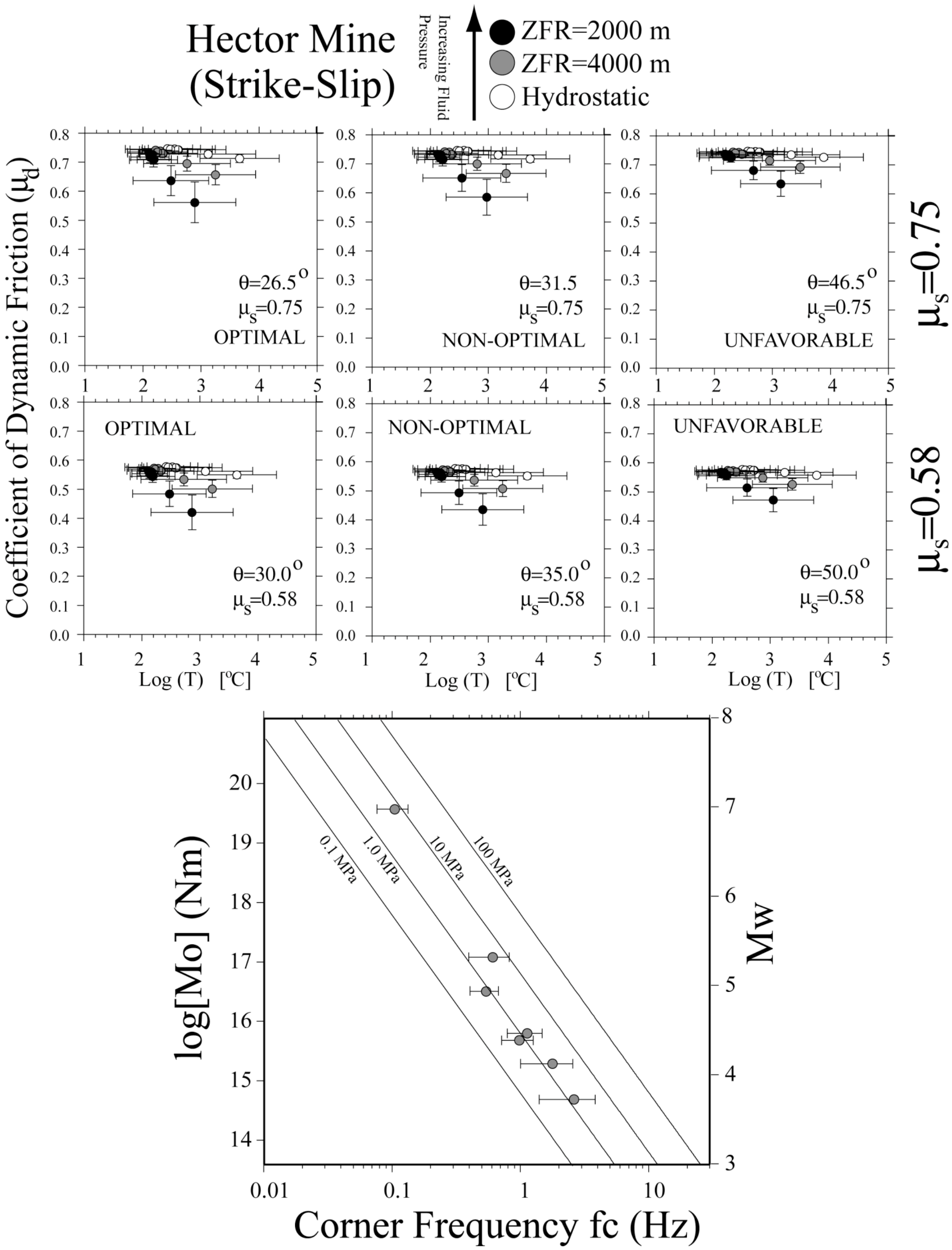


**Figure A7.** Coefficients of dynamic friction for the evens of the Hector Mine seismic sequence, as a function of the fault temperature. Darker symbols indicate shallower gradient transition depths, and thus higher pore fluid pressures. We sample two typical coefficients of static friction (0.75 and 0.58), and three possible orientations.

Bottom frame: distribution of the seismic moments and corner frequencies for the sequence. The data set may be consistent with a functional form: $M_0 \propto f_c^{-3}$, with a discontinuity at $M_W 5.5$, or with a functional form: $M_0 \propto f_c^{-3+\varepsilon}$, with $\varepsilon = 0.9 \pm 0.4$.

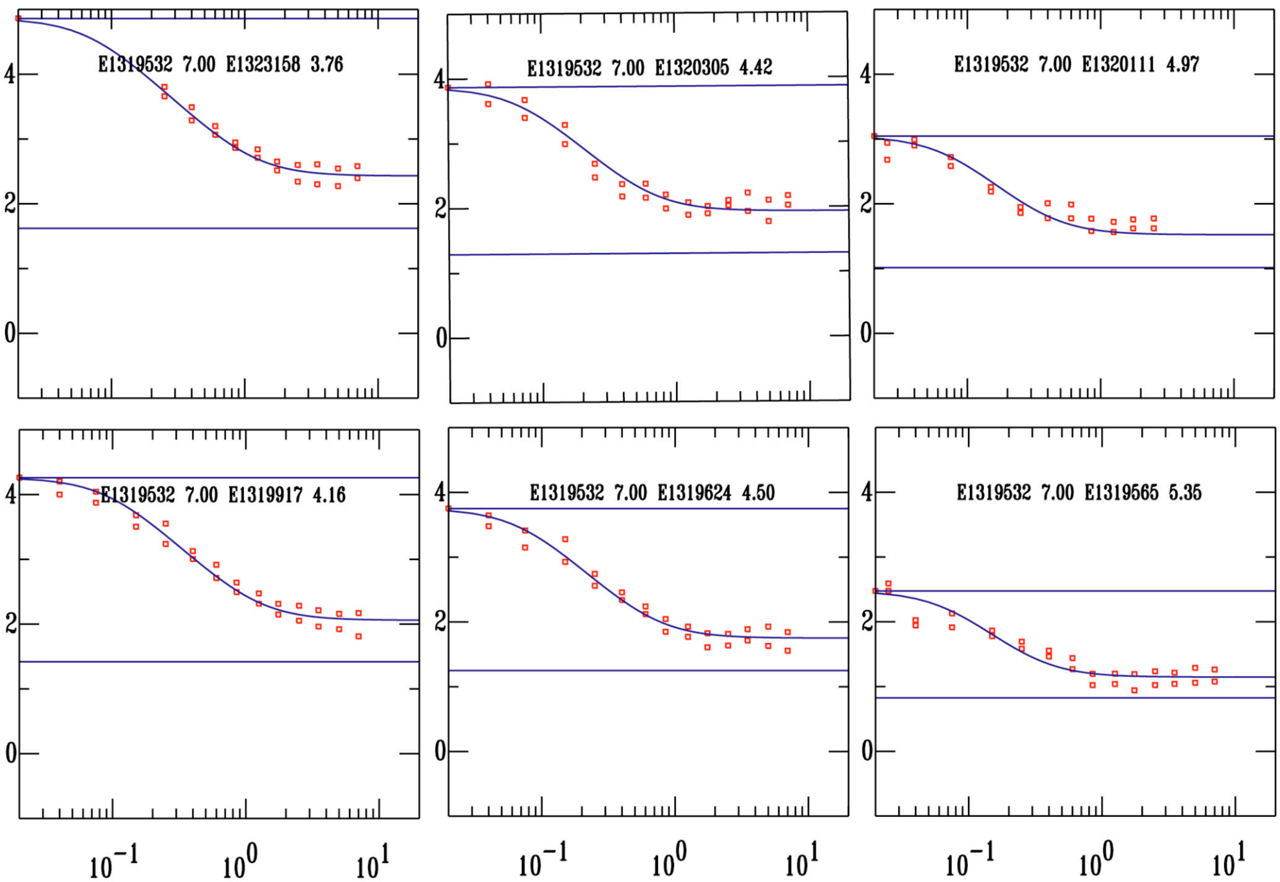


**Figure A8.** Fits between data (red squares) and the theoretical best scaling model (blue curve) for spectral ratios of the Hector Mine seismic sequence. Solid horizontal lines in blue represent the asymptotes expected for self-similar scaling. In the frame of each spectral ratio are indicated both the event identification numbers, with the earthquakes' moment magnitudes.

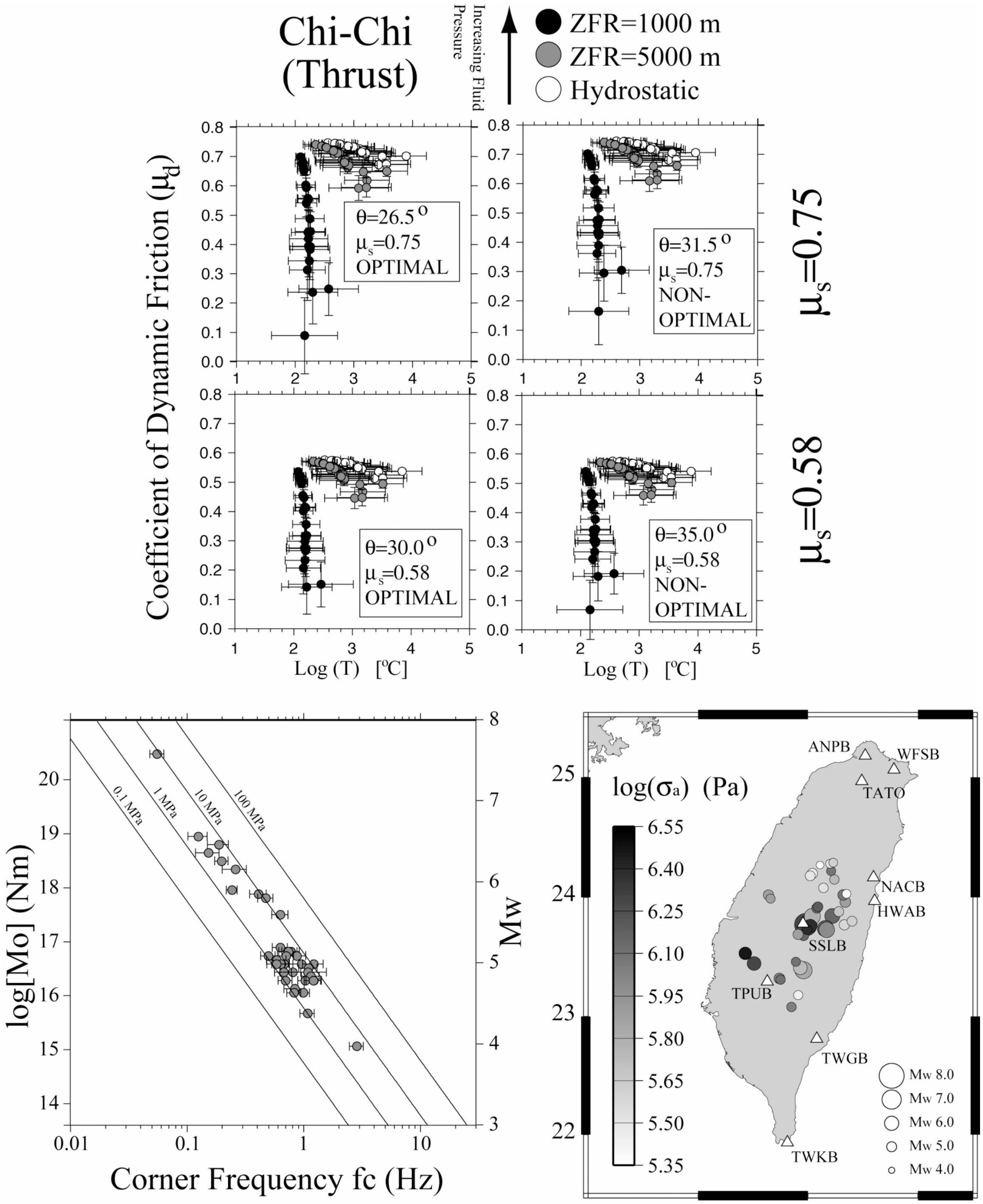


**Figure A9.** Upper frame: coefficients of dynamic friction for the evens of the Chi-Chi seismic sequence, as a function of the fault temperature. Darker symbols indicate shallower gradient transition depths, and thus higher pore fluid pressures. We sample only one typical coefficients of static friction ($\mu_S$=0.75), because there is evidence (Tanikawa and Shimamoto, 2009) for a large coefficient of static friction. We use an optimal dip angle (26.5$^0$) that is very close to the dip of the CMT solution (25$^0$). The high-pressure gradient transition depth was put at 725 m in order to match, on average, the coefficients of dynamic friction obtained in the lab for the Chelungpu fault (Tanikawa and Shimamoto, 2009). Bottom left frame: distribution of the seismic moments and corner frequencies for the sequence. The data set shows a self-similar behavior. Bottom right frame: map of the island, where we plot the locations of the events used here, with an estimate of the logarithm of the apparent stress. The mainshock and the largest aftershocks are characterized by similar apparent stresses.

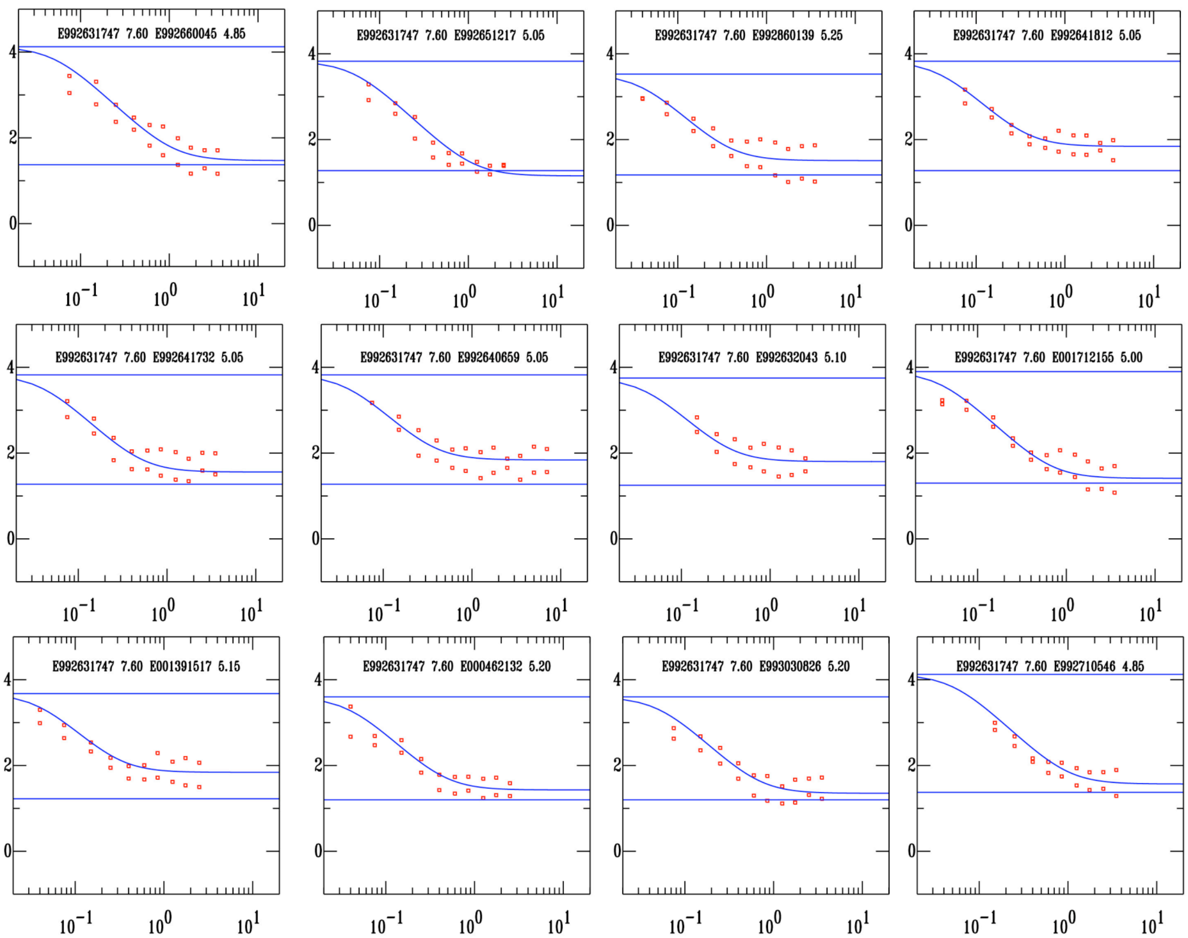


**Figure A10.** Fits between data (red squares) and the theoretical best scaling model (blue curve) for spectral ratios of the Chi-Chi seismic sequence. Solid horizontal lines in blue represent the asymptotes expected for self-similar scaling. In the frame of each spectral ratio are indicated both the event identification numbers, with the earthquakes' moment magnitudes.

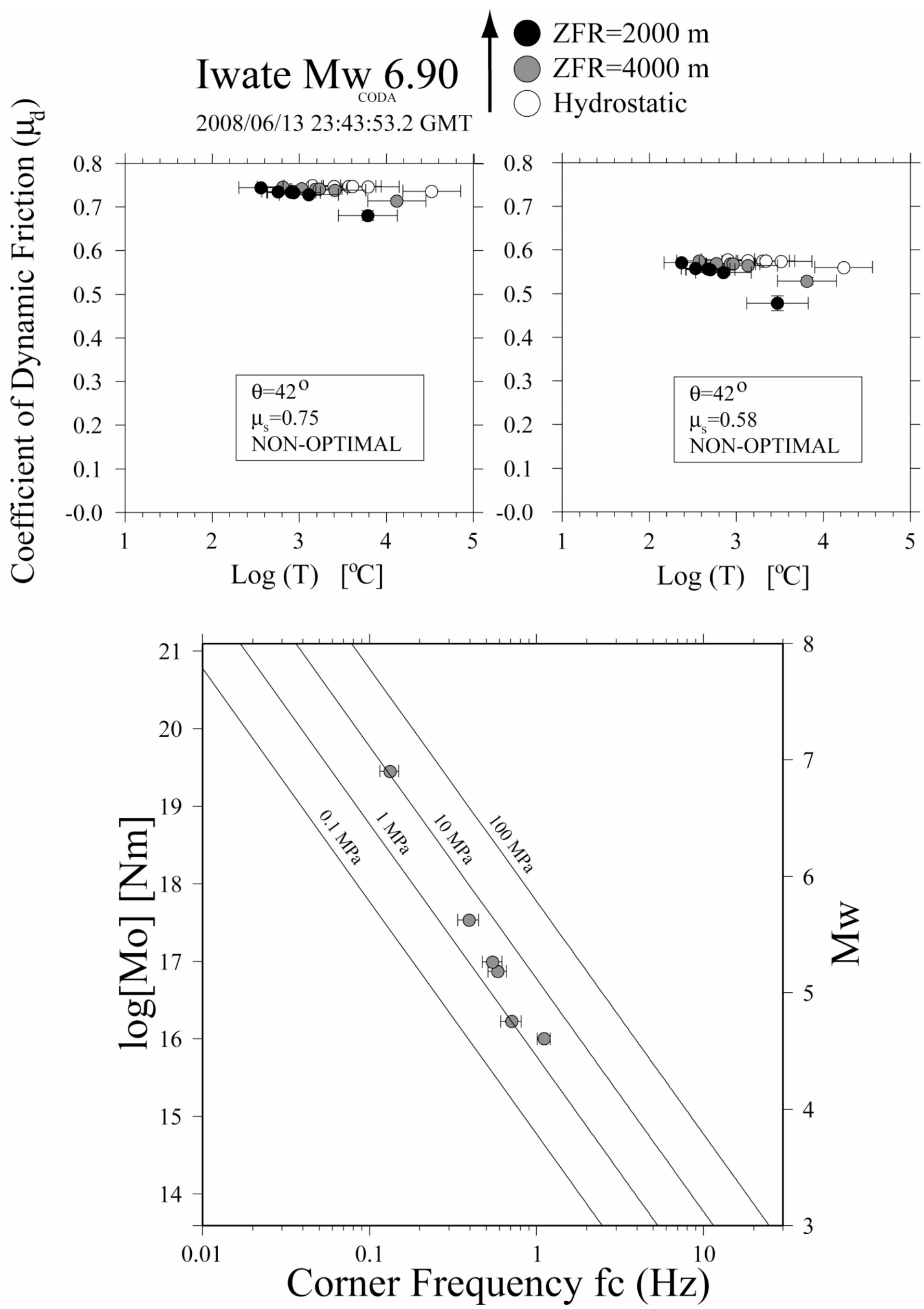


**Figure A11.** Coefficients of dynamic friction for the evens of the Iwate seismic sequence, as a function of the fault temperature. Darker symbols indicate shallower gradient transition depths, and thus higher pore fluid pressures. We sample two typical coefficients of static friction (0.75 and 0.58), and the orientation of the focal mechanism.

Bottom frame: distribution of the seismic moments and corner frequencies for the sequence. The data set may be consistent with a functional form: $M_0 \propto f_c^{-3}$, with a discontinuity at $M_W \approx 5.5 - 6.0$, or with a functional form: $M_0 \propto f_c^{-3+\varepsilon}$, with $\varepsilon > 0$.

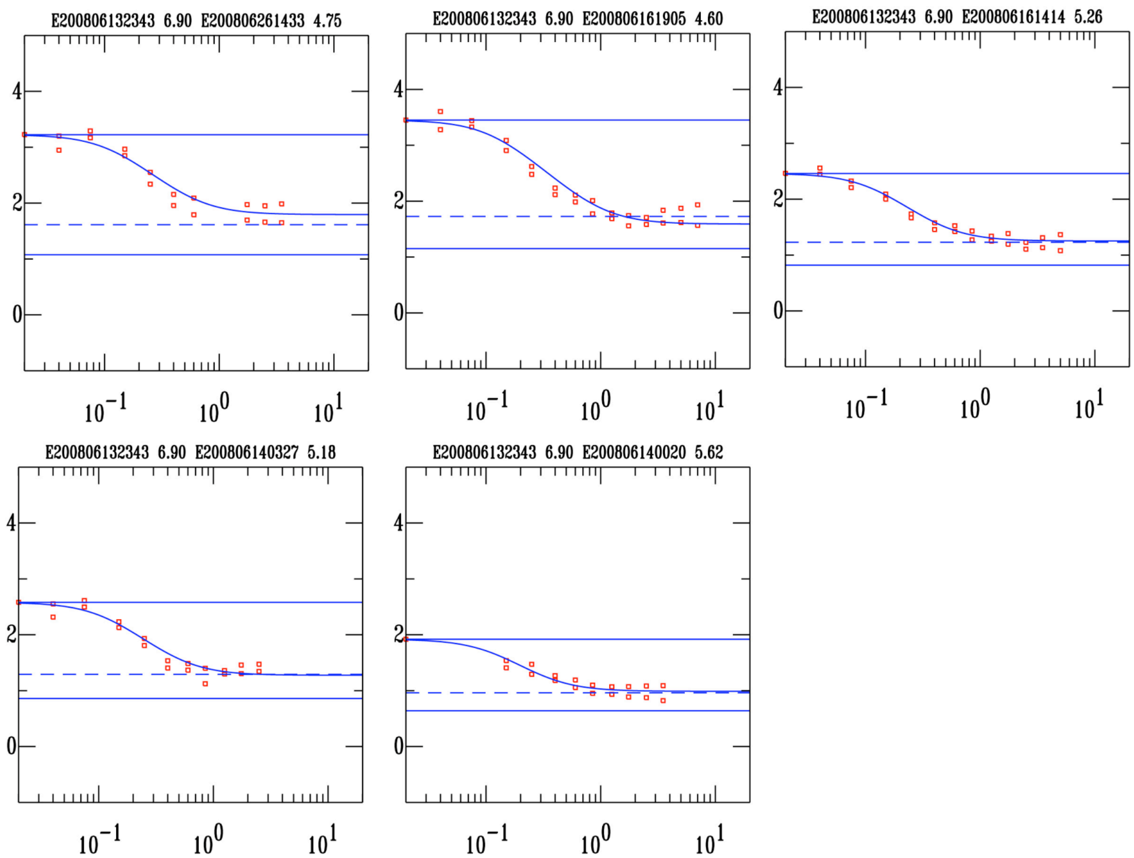


**Figure A12.** Fits between data (red squares) and the theoretical best scaling model (blue curve) for spectral ratios of the Iwate seismic sequence. Solid horizontal lines in blue represent the asymptotes expected for self-similar scaling. In the frame of each spectral ratio are indicated both the event identification numbers, with the earthquakes' moment magnitudes.